
Properties of environment around AGN and luminous galaxy pairs through HSC wide survey

Yuji SHIRASAKI^{1,2}, Masayuki AKIYAMA³, Yoshiki TOBA^{4,5,6}, Wanqiu HE³ and Tomotsugu GOTO⁷

¹National Astronomical Observatory of Japan, 2-21-1 Osawa, Mitaka, Tokyo 181-8588, Japan

²Department of Astronomical Science, School of Physical Sciences, The Graduate University for Advanced Studies, SOKENDAI, 2-21-1 Osawa, Mitaka, Tokyo 181-8588, Japan

³Astronomical Institute, Tohoku University, 6-3 Aramaki, Aoba-ku Sendai, Miyagi 980-8578, Japan

⁴Department of Astronomy, Kyoto University, Kitashirakawa-Oiwake-cho, Sakyo-ku, Kyoto 606-8502, Japan

⁵Academia Sinica Institute of Astronomy and Astrophysics, 11F of Astronomy-Mathematics Building, AS/NTU, No.1, Section 4, Roosevelt Road, Taipei 10617, Taiwan

⁶Research Center for Space and Cosmic Evolution, Ehime University, 10-13 Dogo-Himata, Matsuyama, Ehime 790-8577, Japan

⁷Institute of Astronomy and Department of Physics, National Tsing Hua University, Hsinchu 30013, Taiwan

*E-mail: yuji.shirasaki@nao.ac.jp

Received ; Accepted

Abstract

We investigated the properties of AGN environments, particularly environments where the association of luminous galaxies (LGs) is found within 4 Mpc from AGNs with redshifts of 0.8 – 1.1. For comparison, three additional AGN environments, (namely, AGNs of all types, type 1 AGNs with X-ray and/or radio detection, and type 2 AGNs) and an environment of blue M_* , characteristic luminosity of the Schechter function, galaxies were investigated. The cross-correlation function with the surrounding galaxies was measured and compared between the AGN and blue galaxy samples. We also compared the distributions of color, absolute magni-

tude, and stellar mass of the galaxies around such target objects. The properties of clusters detected using surrounding galaxies selected based on a photometric redshift were examined and compared for different samples. The target AGNs were drawn from the Million Quasars (MILLIQUAS) catalog, and the blue galaxies were drawn from six redshift survey catalogs (SDSS, WiggleZ, DEEP2, VVDS, VIPERS, and PRIMUS). The galaxies used as a measure of the environment around the targets are drawn from S18a internal data released by the Hyper Suprime-Cam Subaru Strategic Program (HSC-SSP). We found that, among the five AGN and blue galaxy samples considered, the environment of AGN-LG pairs is the most enriched with luminous galaxies. We also found an enhancement in the number of mass-selected clusters in the AGN-LG pair sample against those in the other samples. The results obtained in this study indicate that existence of multiple clusters is the major driver in the association of AGNs and LGs, rather than a single large-mass dark matter halo hosting the AGN.

Key words: galaxies: active — large-scale structure of universe — quasars: general

1 Introduction

The ubiquity of super massive black holes (SMBHs) at the centers of galaxies has been recognized through the observation of nearby galaxies (Richstone et al. 1998; Kormendy & Ho 2013). Various processes are believed to be relevant to the feeding of SMBHs, including the following: a secular evolution caused by gravitational instability inside a galaxy (Kormendy & Kennicutt 2004), a minor/major merger (Sanders et al. 1988; Di Matteo et al. 2005; Hopkins et al. 2008), a quiescent accretion of hot halo gas (Kereš et al. 2009; Fanidakis et al. 2013), the ram pressure (van den Bosch 2008), and tidal force feeding.

Low and intermediate luminosity AGNs are thought to be mostly caused by a secular evolution, and the most luminous AGNs, i.e., QSOs, are triggered by major mergers (e.g. Treister et al. 2012; Menci et al. 2014). Several observations, however, have indicated that the major mergers are not a dominant mechanism for the triggering of a QSO (e.g. Villforth et al. 2017). The main driving mechanism of QSO activity remains open to debate.

One of the powerful ways to distinguish among the possible mechanisms is the environmental analysis of the AGN (e.g. Coil et al. 2007, 2009; Hickox et al. 2009, 2011; Krumpel et al. 2012, 2018; Komiya et al. 2013; Ikeda et al. 2015; Shirasaki et al. 2018; He et al. 2018). Mergers

are likely to occur in a high density region except for a cluster core, where the relative velocity is too high to merge or interact with other galaxies and trigger a gas accretion. The quiescent accretion of hot halo gas may be found in a cluster core, whereas ram pressure feeding occurs in the in-fall region of a cluster and between clusters that are in the process of merging. Thus, knowing the positional relationship between AGNs and high density regions provides a hint to solve the present problem.

The Hyper Suprime-Cam Subaru Strategic Program (HSC-SSP) is a multi-band imaging survey conducted using the HSC (Miyazaki et al. 2012, 2018; Komiyama et al. 2018; Kawanomoto et al. 2018; Furusawa et al. 2018). The dataset of the wide layer covers 1,400 deg², and the limiting magnitude is as deep as $r \sim 26$. Thus, it provides a powerful tool to investigate the environment of an AGN with unprecedented statistics.

Using the first-year dataset of HSC-SSP, Shirasaki et al. (2018) measured the clustering of galaxies around AGNs, and found that luminous galaxies are strongly clustered around them. Their results indicate that the cross-correlation length increases from 7 h^{-1} Mpc at approximately $M_{\lambda 310} = -19$ mag to $> 10 h^{-1}$ Mpc beyond $M_{\lambda 310} = -20$ mag, where $M_{\lambda 310}$ represents the absolute magnitude measured at the rest frame wavelength of 310 nm. At approximately $M_{\lambda 310} = -22$ mag, it reaches 30 h^{-1} Mpc, which is too large to be attributed solely to the mass of the host dark matter halo; the expected number density of dark matter haloes clustered at the same level of those luminous galaxies is too low to produce the observed number of luminous galaxies. Thus, the large clustering of luminous galaxies should be attributed in part, or mostly, to other properties related with their environment.

Shirasaki et al. (2018) also showed that the luminosity function measured around AGNs can be described using a smaller (brighter) characteristic luminosity, M_* , parameter when fitted with the Schechter function (Schechter 1976). This indicates that the mass assembly of galaxies rapidly progress around some of the AGNs and, as a result, AGNs are more likely to be associated with luminous galaxies. As the strong cross-correlation between AGNs and luminous galaxies extends over the ~ 10 Mpc scale, the mechanism should be related to the activity in a large-scale structure, such as a cluster-cluster interaction, enhanced galaxy merger, or gas inflow at a saddle point in the filament, among other possibilities. To understand what mechanism is relevant to the simultaneous occurrence of an AGN activity and the evolution of galaxies around it, it is crucial to investigate the properties of the environment of the AGN, particularly an AGN with an association of luminous galaxies.

For this reason, we investigated the environmental properties around AGNs associated with luminous galaxies (LGs) within a distance of 4 Mpc (namely, AGNs paired with LGs,

which are hereinafter referred to as AGN-LG pairs) by comparing with the environment of four different target objects: blue galaxies, AGNs as a whole, type 1 AGNs through X-ray and/or radio detection (AGN type 1 XR), and type 2 AGNs. To determine the distance scale for selecting AGN-LG pairs we examined the clustering of galaxies around the pairs for three different scales, 2 Mpc, 4 Mpc and 8 Mpc, and found that the significance of the excess of clustering against the whole AGN sample was the largest for the sample selected with 4 Mpc scale. Thus we decided to use 4 Mpc for selecting AGN-LG pairs for this study. The blue galaxies are used as a proxy to the environment of an ordinary galaxy.

Because different clustering properties have been reported for different types of AGNs by numerous authors (e.g. Hickox et al. 2009; Allevato et al. 2014; Mendez et al. 2016), we also carried out a comparison between different types of AGNs. In those studies, AGNs selected by X-ray and radio observations shows larger clustering compared to the other types of AGNs. Thus the AGN type 1 XR sample is used as a representative of AGNs in higher overdensity environments. The clustering of LGs around the AGNs increases at higher redshifts (Shirasaki et al. 2018), whereas the availability of galaxies measured for their redshift is limited to a redshift of ~ 1.1 for the galaxy redshift catalogs used in this work: SDSS DR14 (Abolfathi et al. 2018), WiggleZ final (Drinkwater et al. 2018), DEEP2 DR4 (Newman et al. 2013), VVDS (Févre et al. 2013), VIPERS (Scodreggio et al. 2018), and PRIMUS (Coil et al. 2011; Cool et al. 2013). Thus, the target redshift was set to 0.8–1.1, where the sample size for AGN-LG pairs becomes maximal. From the results obtained through the comparisons, we aim to determine what type of mechanism has an effect on the AGN activity and the formation of LGs around the AGN.

Throughout this paper, we assume a cosmology with $\Omega_m = 0.3$, $\Omega_\lambda = 0.7$, $h = 0.7$, and $\sigma_8 = 0.8$. All magnitudes are given in the AB system. All distances are measured in comoving coordinates. The correlation length is presented in unit of $h^{-1}\text{Mpc}$ to facilitate a comparison with other measurements.

2 Datasets

2.1 Galaxies as a measure of the environment

As a measure of the environment of the AGNs and blue galaxies considered, we used photometric galaxies derived from the HSC-SSP survey. The internal release of the S18a wide layer dataset was used in this analysis. The observed locations and effective area of the S18a wide dataset are summarized in Table 1. The typical depths of the observation are 26.6, 26.2, 26.2, 25.3, and 24.5 for the g , r , i , z , and y bands, respectively. The details of the survey itself are described

Table 1. Summary of the survey area

Field name	Approx. center coordinates	S^a deg ²
WIDE12H/GAMA15H	13 ^h 10 ^m +00°00′	263.1
VVDS	23 ^h 20 ^m +02°00′	248.4
GAMA09H	09 ^h 35 ^m +02°00′	196.9
XMM-LSS	02 ^h 15 ^m −01°00′	132.5
HECTOMAP	15 ^h 00 ^m +43°30′	98.4
WIDE01H	01 ^h 15 ^m +01°00′	27.9
AEGIS	14 ^h 17 ^m +52°30′	2.1
Total		969.3

^a Effective area of each survey field of S18a internal release.

in Aihara et al. (2017), and the content of the S18a dataset is provided in Aihara et al. (2019).

The S18a dataset was analyzed through the HSC pipeline (version 6.5.1/6.5.3/6.6) developed by the HSC software team (Bosche et al. 2018) using codes from the Large Synoptic Survey Telescope (LSST) software pipeline (Ivezić et al. 2008; Axelrod et al. 2010; Jurić et al. 2015). Photometric and astrometric calibrations were conducted based on data obtained from the Panoramic Survey Telescope and Rapid Response System (Pan-STARRS) 1 imaging survey (Magnier et al. 2013; Schlafly et al. 2012; Tonry et al. 2012).

The photometric magnitude used in this work is a CModel magnitude. The galactic reddening was corrected according to the dust maps derived by Schlegel et al. (1998). There is a known issue regarding the CModel magnitude that, for some objects, the CModel magnitude has a significantly large deviation from the other magnitude measurements, such as the magnitude in the aperture. We checked the effect of such errors on our analysis, and found that it is negligibly small.

The HSC sources satisfying the criteria summarized in table 2 were selected. The criteria were tested for all four *griz*-bands. Because the observations in the *y*-band are shallower than those in the other bands, the detection in the *y*-band was not required to avoid bias against redder galaxies. In addition to these selection criteria, other selections such as those based on the absolute magnitude space and photometric redshift (photo-*z*) were applied. These additional selections will be described in the analysis method and results section.

The S18a dataset also provides photo-*z* and the stellar mass for most of the sources as an ancillary catalog (Tanaka et al. 2018). We utilized the photo-*z* and stellar masses calculated using the Direct Empirical Photometry code (DEmp: Hsieh & Yee 2014). The photo-*z* and stellar mass were computed from HSC photometry using the empirical fitting method independently.

Table 2. Summary of selection criteria of HSC sources

column name	constraint	explanation of the column
[girz]_pixelflags_edge	IS NOT TRUE	Source is outside usable exposure region
[griz]_pixelflags_saturatedcenter	IS NOT TRUE	Saturated pixel in the Source center
[griz]_pixelflags_bad	IS NOT TRUE	Bad pixel in the Source footprint
[griz]_cmodel_flag	IS NOT TRUE	cmodel fit failed
[griz]_cmodel_mag	IS NOT NULL	cmodel magnitude
[griz]_cmodel_mag	BETWEEN 1 AND 90	
[griz]_cmodel_magsigma	IS NOT NULL	uncertainty of cmodel magnitude
[griz]_cmodel_magsigma	BETWEEN 0 AND 0.2	
i_mask_s18a_bright_objectcenter	IS NOT TRUE	Source center is close to BRIGHT_OBJECT pixels
isprimary	IS TRUE	true if this is a primary data of this object

[griz] in the column name means that any corresponding columns of four HSC bands (g, r, i , and z) were tested for the selection. All columns except for `i_mask_s18a_bright_objectcenter` are from the `s18_wide.forced` table. In addition, `i_mask_s18a_bright_objectcenter` is from the `s18_wide.masks` table.

In figure 1 we compared the photo- z (z_{photo}) with the spectroscopic redshifts (spec- z , z_{spect}) drawn from SDSS DR14 (Abolfathi et al. 2018), WiggleZ final (Drinkwater et al. 2018), DEEP2 DR4 (Newman et al. 2013), VVDS (Févre et al. 2013), VIPERS (Scodreggio et al. 2018), and PRIMUS (Coil et al. 2011; Cool et al. 2013) The matching of the objects were performed by searching nearest neighbors within 1 arcsec from the HSC sources. The comparison were made for HSC sources with i -band magnitudes between 22 and 24 mag with average magnitude of 22.6 mag. This magnitude range was chosen to match with a typical brightness range in this work. The standard deviation of the differences is 0.084 after three sigma clipping for objects of $z_{\text{photo}} = 0.8 - 1.1$, and the fraction of outlier is 18% if it is defined as the fraction of $|z_{\text{spect}} - z_{\text{photo}}| > 0.1$.

The averages of errors in the estimates of stellar mass are plotted in figure 2 for lower and upper bound of 68% confidence interval. The error of stellar mass is 0.1 dex at $M_s = 10^9 - 10^{11} M_{\odot}$, whereas the error of lower bound rapidly increases above $10^{11.5} M_{\odot}$.

2.2 AGN samples

The AGNs were drawn from the Million Quasars (MILLIQUAS) catalog v5.7 2019 update (Flesch 2015). MILLIQUAS is a compilation of identified AGNs/QSOs or their candidates from various studies and QSO catalogs, which have reached 1 983 749 in number. We selected AGNs for which spec- z are within the range of 0.8–1.1 and that are well contained within the area of the S18a HSC-SSP wide dataset. The selected AGNs were further filtered according to

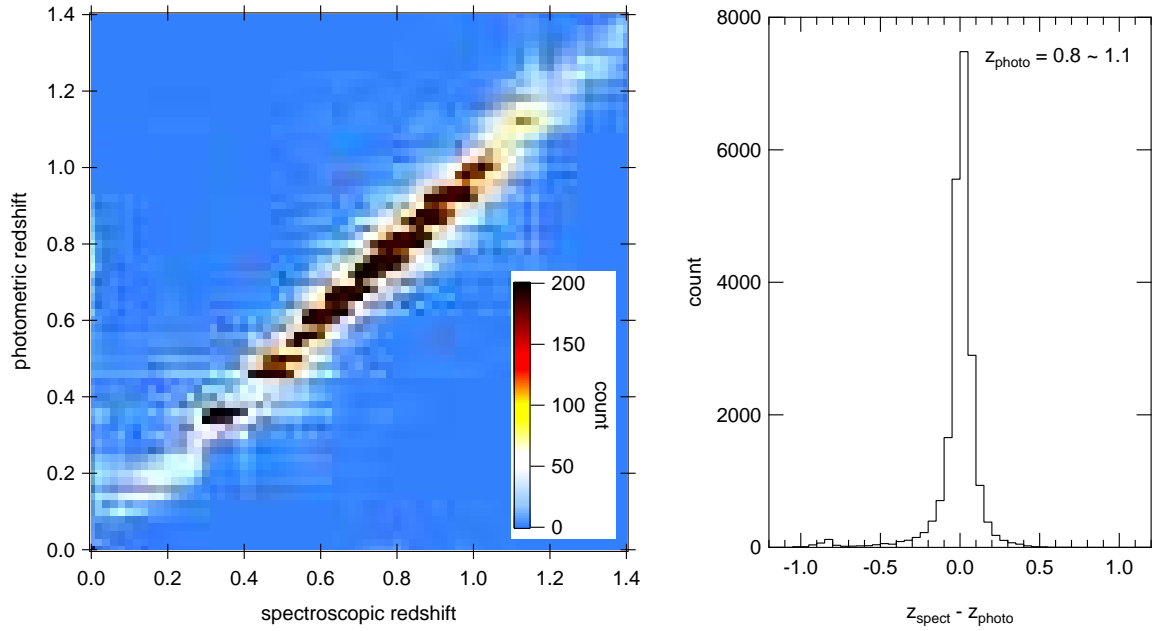


Fig. 1. Comparison of photo- z derived from HSC photometric data and spec- z drawn from redshift catalogs of SDSS DR14, WiggleZ, DEEP2 DR4, VVDS, VIPERS, and PRIMUS. The left panel shows a density plot of photo- z vs spec- z . The right panel shows a histogram of difference between the two redshifts for objects at photo- z of 0.8–1.1.

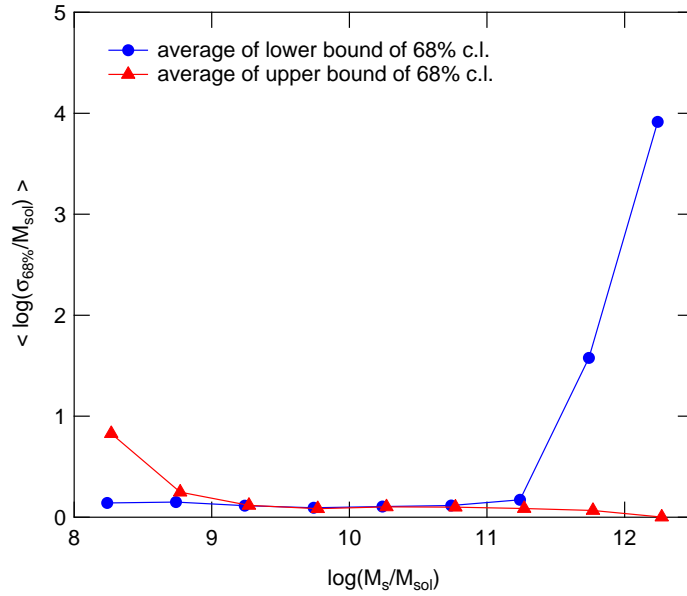


Fig. 2. Averages of errors in the estimates of stellar mass for lower (solid circles connected with lines) and upper (solid triangles connected with lines) bound of 68% C.L. interval in $\log M_s/M_{\odot}$.

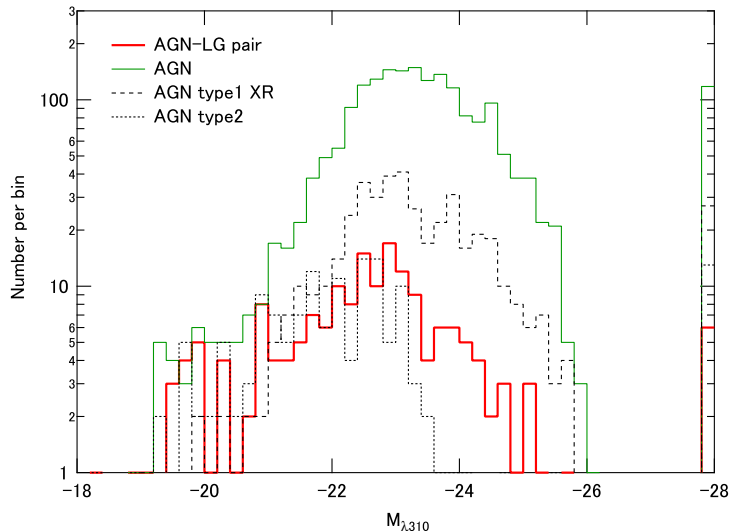


Fig. 3. Distribution of absolute magnitude $M_{\lambda 310}$ for each AGN sample. AGNs for which the absolute magnitude was not measured owing to saturation or other selection criteria are counted at the brightest bin.

the conditions of the HSC sources around them and their proximity, as described in section 2.4.

We extracted four AGN samples, namely, AGNs from all types (hereinafter referred to as a whole AGN sample or simply an AGN sample), AGNs with an associated nearby luminous galaxy ($M_{\lambda 310} < -21$) (an AGN-LG pair sample or simply an AGN-LG sample), type 1 AGNs through X-ray or radio emissions (an AGN type 1 XR sample), and type 2 AGNs (an AGN type 2 sample). The absolute magnitude $M_{\lambda 310}$ distributions for these AGN samples are shown in figure 3. The method for calculating the absolute magnitude is the same as that described in Shirasaki et al. (2018), and is detailed in the following section as well. For some of the AGNs, we were unable to measure $M_{\lambda 310}$ owing to a saturation in the HSC photometry or other selection criteria preventing the source to be analyzed. Such AGNs are counted at the brightest bin at $M_{\lambda 310} = -28.0 - -27.8$.

To see the difference in the distributions of the absolute magnitude between the AGN-LG sample and whole AGN sample, their number ratios are plotted in figure 4. The result shows that the AGNs in the AGN-LG sample are dominated by lower luminosity AGNs as compared to those in the whole AGN sample.

In constructing the sample of AGN-LG pairs, LGs were drawn from the following six redshift survey catalogs: SDSS DR14 (Abolfathi et al. 2018), WiggleZ final (Drinkwater et al. 2018), DEEP2 DR4 (Newman et al. 2013), VVDS (Févre et al. 2013), VIPERS (Scodreggio et al. 2018), and PRIMUS (Coil et al. 2011; Cool et al. 2013). These catalogs were also used for constructing the blue galaxy sample.

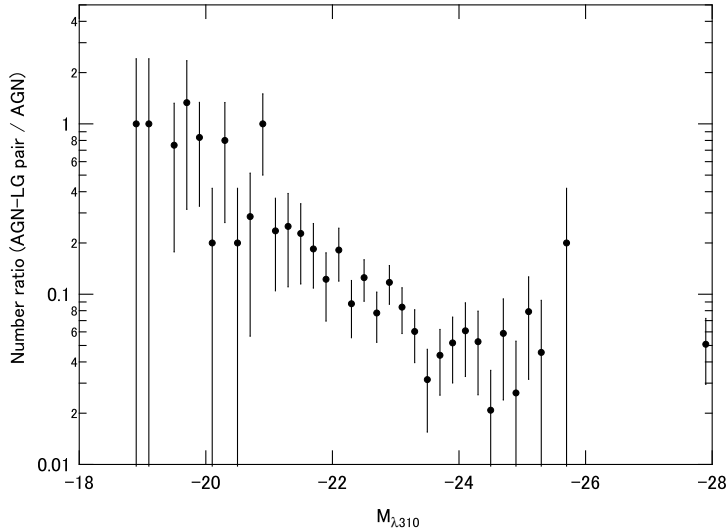


Fig. 4. Ratio of the number of AGNs in the AGN-LG sample to their number in the whole AGN sample at each absolute magnitude $M_{\lambda 310}$.

The absolute magnitude $M_{\lambda 310}$ in these catalogs was measured for each galaxy, as described in the following section. The counterpart LGs were searched within 4 Mpc in projected distance from the AGN and 5 Mpc in the line-of-sight direction determined from the redshift measurement. The line of sight distance was set 1 Mpc larger to accommodate the redshift uncertainty. The typical uncertainties of redshift are 0.00006 (DEEP2), 0.0003 (SDSS, WiggleZ), 0.001 (VIPERS), 0.0014 (VVDS), and 0.01 (PRIMUS). Considering that 50% of the the AGN-LG pairs come from the DEEP2, SDSS, or WiggleZ catalog, the margin of distance was chosen to be 1 Mpc, which corresponds to the redshift interval of 0.0004. The distribution of the separation distances to the brightest LGs is shown in figure 5.

To reduce the effect of the redshift dependence of the clustering and other environmental properties in the comparison among the different samples, a redshift-match-selection was carried out by selecting the same relative number of target objects at random for each redshift range of $z = 0.8-0.9$, $0.9-1.0$, and $1.0-1.1$. The relative numbers were determined from the numbers in the AGN-LG sample, which are 76, 54, and 50 for those redshift ranges, respectively. The details of the sample selections other than those described herein are provided in section 2.4.

The numbers of AGNs for each sample are summarized in table 3 for each AGN type. As was previously shown in figure 4, AGNs in the AGN-LG sample are biased toward lower luminosity AGNs, classified as “AGN” rather than “QSO”, when compared to those in the whole AGN sample. The classification between AGN and QSO in the MILLIQUAS catalog is in principle based on their morphology (Flesch 2015); The core-dominated objects with no disk seen are classified as QSO and disk dominated ones are classified as AGN. For faint and

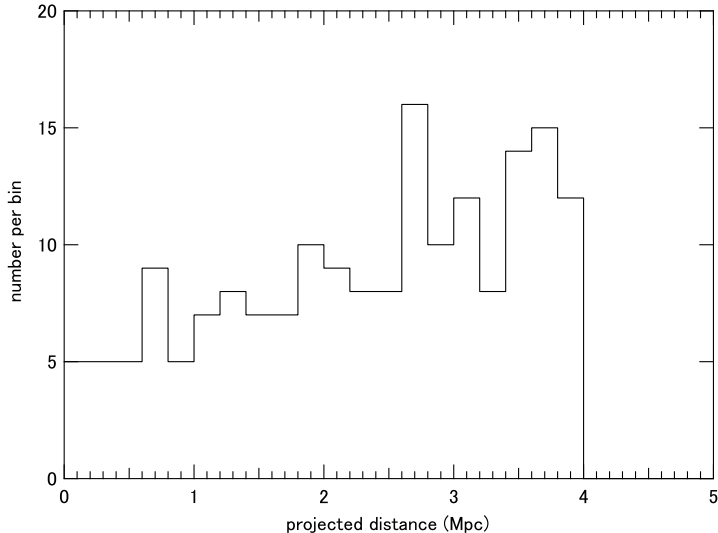


Fig. 5. Distribution of projected separation distance between AGN and an LG in the AGN-LG pair sample.

unresolved objects, the classification is made by their apparent magnitude; The objects brighter than the following magnitude are classified as QSO (Flesch 2015):

$$m = 22 + 5 \log_{10}(z(0.8 + z) - 0.09), \quad (1)$$

where z is a redshift of the object. The QSO-to-AGN ratio for the AGN-LG sample is 3.9:1, whereas that for the whole AGN sample is 25.8:1.

2.3 Blue M_* galaxies

Blue M_* galaxies were drawn from the following six redshift survey catalogs: SDSS DR14, WiggleZ final, DEEP2 DR4, VVDS, VIPERS, and PRIMUS. We selected galaxies located within the HSC-SSP wide area and within the redshift range of 0.8–1.1. This sample is used as a representative of ordinary galaxies located at a relatively smaller density field than those of the AGNs and red galaxies.

We identified the HSC sources corresponding to those galaxies, and measured their color and absolute magnitude using the HSC photometric data. The measurement was made by fitting the galaxy SED templates to the observed SEDs using EAZY software developed by Brammer et al. (2008). The absolute magnitude $M_{\lambda 310}$ was measured at the rest frame wavelength of 310 nm, and the color was defined as $D = M_{\lambda 270} - M_{\lambda 380}$, where $M_{\lambda 270}$ and $M_{\lambda 380}$ are the absolute magnitude at 270 and 380 nm, respectively.

We then selected blue M_* galaxies that satisfy the criteria $M_{\lambda 310} \geq -21$ and $D < 1.4$. As shown in the later results section, the color distribution for galaxies is well represented with

Table 3. Summary of the number of each AGN type for four AGN samples.

	type	label ^a	n_{AGN}^b	$n_{\text{AGN-LG}}^c$	$n_{\text{Type1-XR}}^d$	n_{Type2}^e	
AGN	type I	A	21	11	0	0	
		X-ray	AX	12	4	16	0
	type II	N	11	10	0	17	
		X-ray	NX	27	12	0	36
		Radio	NR	1	0	0	1
	X & Radio	NRX	1	0	0	1	
QSO	type I	Q	1420	37	0	0	
		X-ray	QX	314	93	363	0
		Radio	QR,QR2	53	0	51	0
		X & Radio	Q2X,QRX,QR2X	20	1	20	0
	type II	K	59	7	0	70	
		X-ray	KX	16	4	0	23
		Radio	KR	1	0	0	1
		X & Radio	KRX	0	1	0	1
Total			1956	180	450	150	

^a classification of object in the MILLIQUAS catalog: Q = QSO type-I, A = AGN type-I, K = narrow line QSO type-II, N = narrow line AGN type-II, R = radio association, X = X-ray association, 2 = double radio lobes. ^b number in the whole AGN sample. ^c number in the AGN-LG pair sample. ^d number in the AGN type 1 XR (X-ray and/or radio detection) sample. ^e number in the AGN type 2 sample.

Table 4. Summary of the number of galaxies from each survey for the blue galaxy sample .

SDSS	WiggleZ	DEEP2	VVDS	VIPERS	PRIMUS	total
106	56	430	123	946	765	2426

a linear combination of three Gaussian functions, which represent blue clouds, red sequences, and green valley galaxies. The criterion $D < 1.4$ separates most of the red galaxies from the sample.

In addition to the selections based on the properties of the target itself, the coverage and uniformity of the HSC sources around the targets were taken into account. As conducted for the AGN samples, a redshift-match-selection was applied. The details of the sample selection other than those explained herein will be described in section 2.4. In total, 2 426 blue M_* galaxies are used in this analysis. The number of galaxies from each survey is summarized in table 4.

2.4 Dataset selection

In the analysis described herein, we treated each target object (AGN or blue galaxy) and its surrounding HSC sources as a set. Hereafter, we refer to the unit of the dataset simply as a dataset. In this section, we describe the criteria to include in the datasets for analysis.

To homogenize the environments of the target objects as much as possible and avoid an edge effect of the survey boundary, we selected target objects that are well within the survey footprint. To do so, we measured the radial distribution of random sources from the position of the target objects. The random source catalog is available for every data release. The random sources were generated with a density of 100 per square arcmin inside the survey footprint, allowing us to estimate the fraction of unobserved or masked regions by counting the random sources.

We selected the random sources adapting the same criteria adapted to the real data if applicable. Their radial distribution was measured in annuli spaced by 0.2 Mpc out to 10 Mpc from the targets. We kept only those targets around which $>60\%$ of the area of all annuli at ≥ 2 Mpc and $>80\%$ of the area at <2 Mpc were included in the survey footprint and not masked for bright sources. The procedure to build and validate the bright-star masks for the HSC-SSP survey is described in Coupon et al. (2018). The datasets that passed this selection numbered 2 740 for the AGNs and 5 222 for the blue galaxies.

The spatial uniformity of the HSC sources around the targets was also examined to identify the datasets that are significantly affected by a high-density foreground region, spurious sources around bright stars, and so on. For this purpose, we calculated two parameters for the radial number density distribution of the galaxies χ^2 and σ_{\max} , where χ^2 is a square sum of the deviation from the number density distribution fitted to the observed data using equation (5), which is derived in section 3.1, where σ_{\max} is the maximum deviation from the density distribution. The adapted criteria for these parameters are as follows: $\chi^2/n \leq 4$ and $\sigma_{\max} \leq 6$. These criteria was chosen to remove a few % of the datasets that deviate the most from a uniform distribution. We checked the effect of these criteria to the estimate of cross-correlation length and confirmed that difference between the cross-correlation lengths calculated for the datasets for which these selection are adapted or not is within the statistical error. The datasets that passed all selections described above totaled 2 720 for the AGNs and 5 126 for the blue galaxies.

In the analysis adapted for this study, it is crucial to construct the datasets such that the contribution from the foreground and background galaxies are smeared out by stacking the radial number distribution of the galaxies. To avoid stacking numerous identical fields, we selected the target objects so that they have no more than one other target object within

Table 5. Summary of the number, median redshift, and median absolute magnitude in the sample for each target type and each redshift group.

z^a	sample type	n^b	\bar{z}^c	$\tilde{M}_{\lambda 310}^d$
0.8–0.9	AGN	826	0.85	−23.0
	blue galaxy	1024	0.85	−20.6
	AGN-LG pair	76	0.85	−22.3
	AGN type 1 XR	190	0.84	−22.8
	AGN type 2	63	0.85	−21.7
0.9–1.0	AGN	587	0.95	−23.4
	blue galaxy	728	0.93	−20.7
	AGN-LG pair	54	0.96	−22.9
	AGN type 1 XR	135	0.96	−23.2
	AGN type 2	45	0.96	−22.4
1.0–1.1	AGN	543	1.05	−23.8
	blue galaxy	674	1.04	−20.7
	AGN-LG pair	50	1.03	−22.9
	AGN type 1 XR	125	1.05	−23.8
	AGN type 2	42	1.04	−22.6
0.8–1.1	AGN	1956	0.92	−23.3
	blue galaxy	2426	0.92	−20.7
	AGN-LG pair	180	0.91	−22.6
	AGN type 1 XR	450	0.93	−23.2
	AGN type 2	150	0.94	−22.1

^a redshift range. ^b number of datasets. ^c median redshift.

^d median absolute magnitude $M_{\lambda 310}$. The median redshift and absolute magnitude for AGN-LG pair are calculated for the AGN.

4 Mpc. This selection was adapted for each redshift bin, which was divided into $z = 0.8\text{--}0.9$, $0.9\text{--}1.0$, and $1.0\text{--}1.1$. The datasets that passed all selections described above numbered 2 622 for the AGNs and 4 262 for the blue galaxies.

To reduce the effect of the redshift dependence in the comparison of the environmental properties, we selected the dataset such that the relative number of datasets for three redshift bins becomes the same among the five target groups. The final numbers of datasets that passed all selections are summarized in table 5 along with the median redshifts and absolute magnitudes of the datasets. The numbers of the datasets broken down by the HSC survey fields are also summarized in table 6.

Table 6. Summary of the number of the datasets for each target type and HSC

survey field.					
field name	n_{AGN}^a	n_{G}^b	$n_{\text{AGN-LG}}^c$	$n_{\text{Type1-XR}}^d$	n_{Type2}^e
WIDE12H/GAMA15H	583	36	3	70	31
VVDS	490	626	38	58	13
GAMA09H	259	252	18	42	61
XMM-LSS	376	1358	102	211	44
HECTOMAP	166	0	3	26	0
WIDE01H	67	1	2	28	0
AEGIS	15	153	14	15	1

^a number in the whole AGN (for all types) sample. ^b number in the blue galaxy sample. ^c number in the AGN-LG pair sample. ^d number in the AGN type 1 XR (X-ray and/or radio detection) sample. ^e number in the AGN type 2 sample.

3 Analysis method

3.1 Cross-correlation between targets and HSC sources.

The cross-correlation functions between the target objects and HSC sources were calculated using the method described in our previous papers (Shirasaki et al. 2011; Komiya et al. 2013; Shirasaki et al. 2016, 2018), which is briefly described herein.

When the redshifts of the target objects are known, we can calculate the number densities of the HSC sources as a function of the projected distance from the target in its redshift plane. Thanks to the clustering properties of galaxies, the galaxies located at the target’s redshift emerge as an excess over the flat distribution of the foreground/background galaxies after stacking the radial number densities for many of the targets.

The cross-correlation function $\xi(r)$ is a measure of the clustering as an excess over random distribution, and is related to the number density $\rho(r)$ of the correlated objects (HSC sources in this analysis) around the target objects (AGN or blue galaxy) as follows:

$$\xi(r) = \rho(r)/\rho_0 - 1, \quad (2)$$

where ρ_0 is the average number density of the correlated objects at the redshift of the targets.

Owing to a lack of precise measurements of the distances to the HSC sources along the line of sight, the projected correlation function $\omega(r_p)$ is measured instead of $\xi(r)$ as follows:

$$\omega(r_p) = \int_{-\infty}^{\infty} \xi(r_p, \pi) d\pi \simeq \frac{n(r_p) - n_{bg}}{\rho_0}, \quad (3)$$

where r_p and π are distance from a target object perpendicular and along to the line of sight, respectively, and $n(r_p) = \int_{-\infty}^{\infty} \rho(r_p, \pi) d\pi$ represents the average surface number density of the

HSC sources at a projected distance r_p , and $n_{\text{bg}} = \int_{-\infty}^{\infty} \rho_0(\pi) d\pi$ represents the average density expected for the case in which all galaxies are uniformly distributed. In deriving the right-hand side expression of equation (3), we used approximation that the effective integral interval is limited to $\pi \sim 0$.

According to the measurements of the galaxy auto-correlation function described in the literature, the correlation function is approximated using a power law function, i.e., $\xi(r) = (r_0/r)^\gamma$. The typical value of the power index γ is 1.8 (e.g. Zehavi et al. 2011; Coil et al. 2008, 2017), and r_0 is termed the correlation length, which is a measure of the galaxy clustering. In this case, $\omega(r_p)$ is expressed as follows:

$$\omega(r_p) = r_p \left(\frac{r_0}{r_p} \right)^\gamma \frac{\Gamma(\frac{1}{2})\Gamma(\frac{\gamma-1}{2})}{\Gamma(\frac{\gamma}{2})}. \quad (4)$$

Equating the right-hand sides of equations (3) and (4), $n(r_p)$ is expressed as follows:

$$n(r_p) = r_p \left(\frac{r_0}{r_p} \right)^\gamma \frac{\Gamma(\frac{1}{2})\Gamma(\frac{\gamma-1}{2})}{\Gamma(\frac{\gamma}{2})} \rho_0 + n_{\text{bg}}. \quad (5)$$

ρ_0 for each dataset is calculated from the luminosity function, which was derived by parametrizing the luminosity functions in the literature, and the completeness function $C(m)$. The detail of the parametrization of the luminosity function and the completeness function is described in Shirasaki et al. (2018) (completeness function is referred to as detection efficiency $DE(m)$ in the reference). The average for all the datasets in the sample provides ρ_0 in equation (5).

The completeness as a function of magnitude $C(m)$ is required to correct for the completeness by multiplying $C(m)$ to the luminosity function model in deriving ρ_0 . It was calculated as a ratio of the observed magnitude distribution $N_{\text{obs}}(m)$ to the model function $N_{\text{org}}(m)$, which is a magnitude distribution expected for an ideal observation of a 100% completeness at any magnitude. For $N_{\text{org}}(m)$, we assumed a broken power law form, and the power law index was determined using data from the HSC-SSP S18a deep survey dataset of the COSMOS field. Next, $C(m)$ was determined for each dataset by fitting $C(m)N_{\text{org}}(m)$ to $N_{\text{obs}}(m)$. For a model of $C(m)$, the same functional form as defined in equation (14) of Shirasaki et al. (2018) was used.

The accuracy of the model function is demonstrated in figure 6 for the magnitude distribution derived from a deep dataset of the COSMOS field. The observed magnitude distribution is well fitted with the broken power law model at magnitudes $m_{\lambda 310} < 26.8$ mag. Since this work is performed at magnitudes $m_{\lambda 310} < 26$ mag for the wide dataset, it is reasonable to assume a broken power law form for $N_{\text{org}}(m)$.

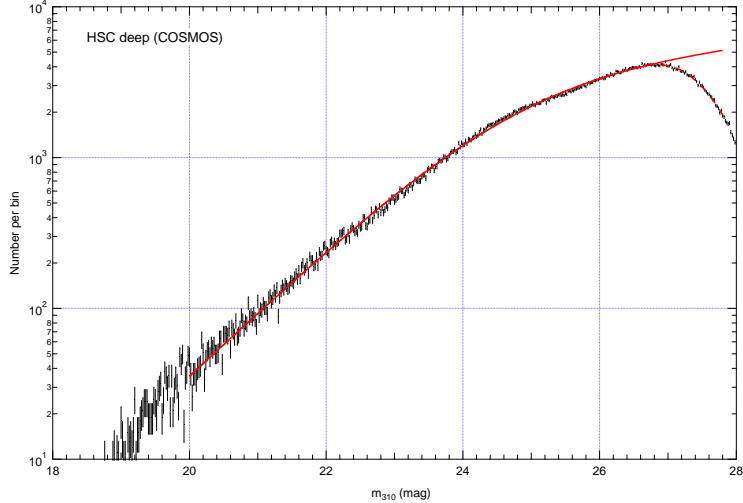


Fig. 6. Distribution of apparent magnitude $m_{\lambda 310}$ derived from a deep dataset of the COSMOS field, where $m_{\lambda 310}$ is an apparent magnitude measured at wavelength $310(1 + 0.9)$ nm in the observer frame, that is 310 nm in the rest frame at redshift 0.9. The solid and dashed lines represent the fitted function expressed in a broken power law function and that multiplied by completeness $C(m)$, respectively.

The radial distributions $n(r_p)$ of the HSC sources were derived by stacking the distributions for all the datasets in the sample, where HSC sources with absolute magnitudes of $M_{\lambda 310} < -19$ mag were used. This threshold magnitude corresponds to an approximately 90% detection (completeness) limit. We applied this analysis for the photo- z selected galaxies, which were constructed by selecting the HSC source whose photo- z are within the range of ± 0.1 from the redshifts of the target object. Although the completeness is reduced by this photo- z selection, background/foreground galaxies are also reduced more efficiently, which results in an increase in the signal to noise ratio of the clustering.

The reduction in the completeness by the photo- z selection was estimated by comparing the projected cross-correlation functions calculated for galaxies with and without photo- z selection. The two projected cross-correlation functions were calculated for the same ρ_0 parameter, which was an estimate for the galaxies without a photo- z selection, and the average ratio between them was then taken to be the reduction rate owing to the photo- z selection. The reduction rate was estimated to be 0.61 for the whole AGN sample, which has large statistical sample size and provides the best signal-to-noise ratio for the clustering, and was also used for the other samples. In figure 7, the two projected cross-correlation functions used to derive the reduction rate are shown.

The effective observational area, which is used for the calculation of $n(r_p)$ and is an area corrected for a dead region affected by a bright source, survey boundary, gaps between observations, or other factors, was estimated using a random catalog. The random catalog,

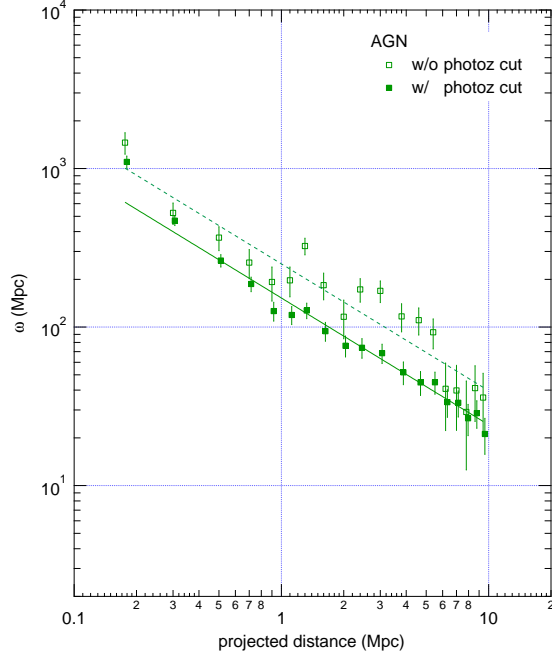


Fig. 7. Projected cross-correlation functions for the whole AGN sample. The open squares indicate the correlation function obtained using all of the galaxies, whereas the solid squares represent that obtained using the photo- z selected galaxies. The same ρ_0 parameter, which was estimated without correcting the reduction through a photo- z selection, is used for both. We use the ratio between them as the correction factor for the photo- z selection.

which was created at random positions avoiding the dead region with number density 100 arcmin^{-1} , was extracted from the S18a database.

We fixed γ to 1.8, and the model function given by the equation (5) is fitted to the observed radial surface densities $n(r_p)$ with two free parameters r_0 and n_{bg} . The fitting was performed by the least square method by weighting each data point with a inverse square of the error determined by Poisson statistics. Since the target objects were selected so as to avoid overlap of the environment regions among them as much as possible, each bin of $n(r_p)$ is almost independent from each other and the covariance between them is negligible. Thus we ignored the covariance in the fitting. The cross-correlation length is estimated as an optimal solution for the free parameter r_0 . The quoted error is a confidence interval in one sigma unless otherwise stated.

We also cross-correlate the target objects to the cluster of the HSC sources. Because no reliable model is available for the cluster mass function, we simply derive the radial number density of the clusters.

3.2 Color, absolute magnitude, and stellar mass distributions around the targets

Although we do not have spec- z of individual HSC sources, we can statistically estimate the distribution of a property X of the HSC sources located at distance within a few Mpc from the target object. Thanks to the clustering feature of galaxies, their number density increases as we get closer to the target objects. Thus, subtracting the distribution of property X measured in a lower density region from that measured at a higher density region, we can estimate the net distribution of property X for HSC sources associated with the target objects.

Property X can be anything that is measurable for the HSC sources. In this analysis, we investigate the distribution of color, absolute magnitude, and stellar mass of the HSC sources. The color is calculated as the difference between magnitudes at the rest frame wavelengths of 270 and 380 nm, and the absolute magnitude is measured at 310 nm in the rest frame of the target object. As previously described in sub-section 2.3, EAZY software (Brammer et al. 2008) was used to interpolate the SED derived from the HSC photometric data. The stellar mass was obtained from the ancillary catalog available along with the photo- z . We used those calculated using the DEMP code (Hsieh & Yee 2014). The photo- z was used to select HSC sources associated with the target objects.

Although the photo- z selection is useful for increasing the signal to noise ratio of the derived distribution, it distorts the intrinsic distribution owing to the dependence of the completeness on the examined property. Thus the completeness should be corrected taking into account its dependence on the property, when the distribution needs to be compared in an absolute manner, e.g. in a case where it is compared with the luminosity functions derived in literature. The reduction rate by the photo- z selection as a function of the absolute magnitude is estimated by comparing the magnitude distribution obtained for all galaxies (without photo- z selection) with that for the photo- z selected galaxies of the whole AGN sample.

In addition, we also investigated the peak density distribution of the clusters detected as stellar mass density peaks (mass peak clusters) and clusters detected as number density peaks (number peak clusters), which were found using a procedure for detecting peaks in the 2D distribution of the HSC sources.

3.3 Identification of peak locations of galaxy number density and stellar mass density around the targets

As described in section 1, the strong cross-correlation between AGNs and LGs found by Shirasaki et al. (2018) extends over ~ 10 Mpc scale, which indicates that the mechanism is related to the activity in the large-scale structure. A cluster-cluster interaction is one of the

candidates to produce strong cross-correlation in such a large scale. Thus we examined the environment of AGN-LG pairs based on the statistics related to the clusters around them.

The peak locations of the number density and stellar mass density of the HSC sources were detected to select galaxy cluster candidates by searching the local maxima in a blurred density map. The blurred density map was constructed by blurring the positional distribution of the photo- z selected HSC sources using a 2D Gaussian with $\sigma = 1$ Mpc. The stellar mass density map was created by weighting each HSC source with its stellar mass, whereas the number density map was created with an equal weight. The stellar mass was limited to $10^{12} M_{\odot}$ to avoid dominance from a single large stellar mass object with a large uncertainty as shown in figure 2, and thus a stellar mass exceeding $10^{12} M_{\odot}$ was set to $10^{12} M_{\odot}$. We checked that lowering the threshold to $10^{11.5} M_{\odot}$ doesn't affect the result and conclusion. The local sub-peaks found within a 1 Mpc projected distance from the local maximum were removed from the sample.

4 Results

4.1 Cross-correlation between target objects and HSC sources

The cross-correlation between the target objects and the HSC sources were examined for five target types: whole AGN (of all types), blue galaxy, AGN-LG pair, AGN type 1 XR (with detection with X-ray and/or radio signals), and AGN type 2.

The results of the fitting and fixed parameters are summarized in table 7. The cross-correlation functions obtained using the fitting parameter are shown in the left panel of figure 8 for the cases of the whole AGN, blue galaxy, and AGN-LG samples, and in the right panel for the cases of AGN type 1 XR and AGN type 2 samples. The cross-correlation lengths obtained for the five samples are compared in figure 9. The cross-correlation lengths obtained for the whole AGN, AGN type1 XR, and AGN-LG samples are significantly larger than those for the blue galaxy and AGN type 2 samples.

The cross-correlation length for the AGN-LG sample is larger than that for the whole AGN sample by four sigma, and is identical to that for AGN type1 XR sample within the margin of error. The environment of AGN type 2 is similar to that of the blue galaxy, which indicates that the AGNs of this sample are mostly caused by an internal secular mechanism rather than an interaction with the external environment.

Table 7. Fitting parameters of cross-correlation functions between five types of target and

HSC sources						
target type	n^a	$\langle z \rangle^b$	r_0^c	n_{bg}^d	ρ_0^e	γ^f
			$h^{-1}\text{Mpc}$	Mpc^{-2}	10^{-3}Mpc^{-3}	
AGN-LG pair	180	0.93	9.03 ± 0.44	4.807 ± 0.019	3.01	1.8
AGN	1 956	0.93	7.22 ± 0.16	4.695 ± 0.006	2.92	1.8
blue galaxy	2 426	0.93	3.77 ± 0.27	4.747 ± 0.005	3.02	1.8
AGN type-1 RX	450	0.93	8.27 ± 0.31	4.718 ± 0.012	2.90	1.8
AGN type-2	150	0.94	4.77 ± 0.78	4.890 ± 0.020	3.04	1.8

^anumber of target objects. ^baverage redshift. ^ccross-correlation length and its error in one sigma. ^daverage surface number density. ^eaverage space number density of galaxies at a redshift of the targets. ^fpower index fixed to 1.8.

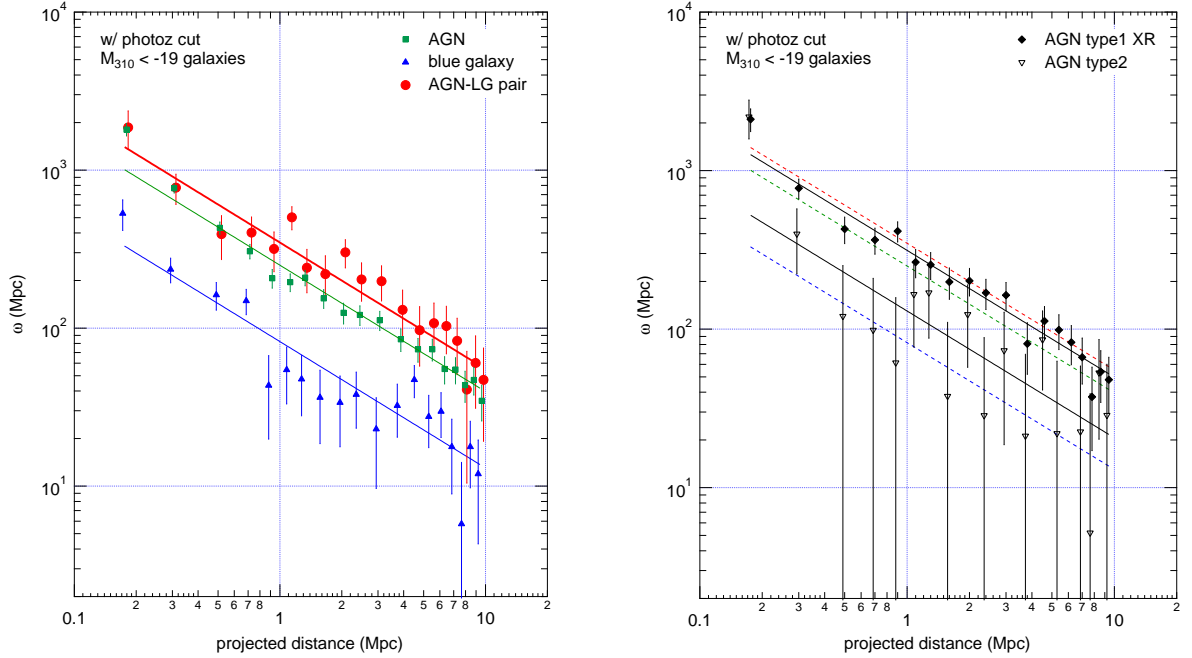


Fig. 8. Left: Projected cross-correlation functions derived for the whole AGN, blue galaxy, and AGN-LG pair samples. The solid lines indicate the power law functions fitted to the data points. The photo- z selected galaxies were used and the data were corrected for a reduction in the factor of 0.61. Right: The same plots as the left panel for AGN type 1 XR (X-ray and/or radio detection) and AGN type 2 samples. The solid lines are functions fitted to the data of these two samples, and the dashed lines are functions fitted to the whole AGN, AGN-LG, and blue galaxies, as shown in the left panel with the solid lines.

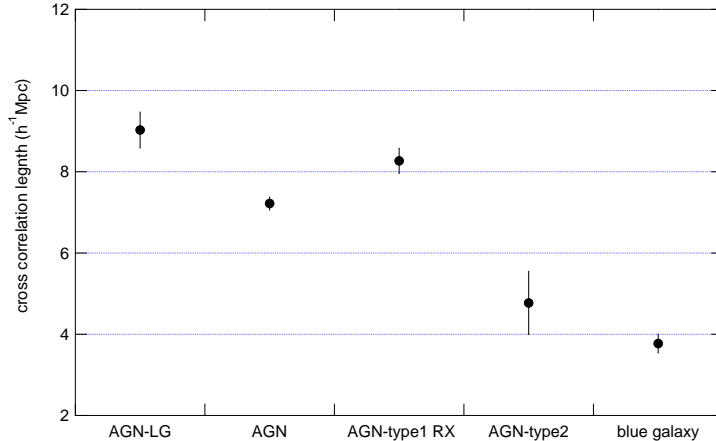


Fig. 9. Cross-correlation lengths measured for the five targets.

4.2 Color distributions

To investigate the difference in the composition of the galaxy types clustered around the three target types, namely, the whole AGN, blue galaxy, and AGN-LG pair, we derived the distribution of galaxy color within the region of 0.2–2.0 Mpc from the targets. For simplicity, in the subsequent analysis, excluding the average number of clusters around the targets, the comparisons are made only for the three samples.

The color distribution was obtained by subtracting the color distribution in a lower density region (7–9.8 Mpc) from that in a higher density region (0.2–2.0 Mpc). The color of each HSC source was calculated according to the method described in section 3.2. The distributions were derived from the HSC sources with a magnitude brighter than $M_{\lambda 320} = -19$ mag and selected based on their photo- z . The results are shown in figure 10.

Each color distribution was fitted with a linear combination of three Gaussian distributions, each of which represents the distribution for red sequence galaxies, blue cloud galaxies, and green valley galaxies. The fitting was first applied to the distributions for the whole AGN sample (left panel of figure 10) by making all nine parameters free. The fitting was then conducted by fixing the mean and standard deviation parameters of the three Gaussians to those determined with the fitting to the whole AGN sample (right panel of figure 10). The fitted function is shown in the figure and the values of the fitting parameters are summarized in table 8.

The number fractions of the green- and red-type galaxies to the total number of galaxies for the three samples are plotted in figure 11. There is no significant difference among them.

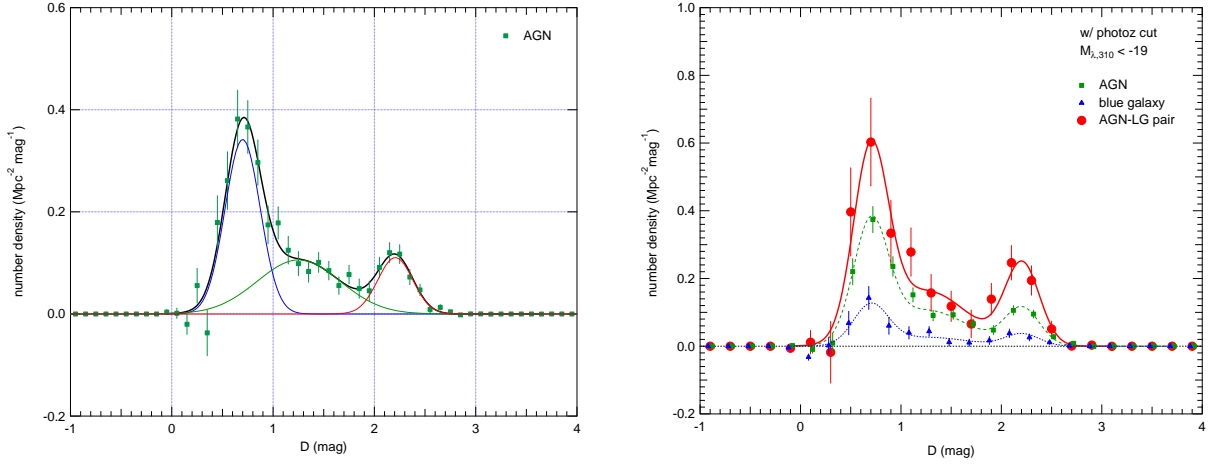


Fig. 10. Left: Color distributions of photo- z selected galaxies around the AGNs of the whole AGN sample. The distributions were fitted using a linear combination of three Gaussian functions, each of which corresponds to blue-, green-, and red-type galaxies. Right: Color distributions of photo- z selected galaxies around AGNs or blue galaxies for the samples of whole AGN, blue galaxy, and AGN-LG pair. The distributions are fitted using three Gaussian functions.

Table 8. Fitting results for the color distributions.

target type	c^a	μ_B^b	σ_B^c	f_G^d	μ_G^b	σ_G^c	f_R^d	μ_R^b	σ_R^c
AGN ^e	0.304 ± 0.016	0.70 ± 0.02	0.17 ± 0.03	0.36 ± 0.13	1.25 ± 0.16	0.41 ± 0.13	0.16 ± 0.03	2.21 ± 0.03	0.17 ± 0.02
AGN ^f	0.304 ± 0.014	0.70	0.17	0.36 ± 0.03	1.25	0.41	0.16 ± 0.01	2.21	0.17
AGN-LG pair ^f	0.506 ± 0.049	0.70	0.17	0.33 ± 0.06	1.25	0.41	0.21 ± 0.03	2.21	0.17
blue galaxy ^f	0.093 ± 0.013	0.70	0.17	0.29 ± 0.08	1.25	0.41	0.17 ± 0.04	2.21	0.17

^ascaling factor of the Gaussian distribution for each galaxy component, ^bmean of the D distribution for each component, and ^cstandard deviation of the D distribution for each component, in which the ^dfraction of green or red galaxy component. ^efitting was applied by making all nine parameters free. ^ffitting was applied by fixing the mean and standard deviation parameters to the values obtained for the nine-parameter fitting to the data of the whole AGN sample.

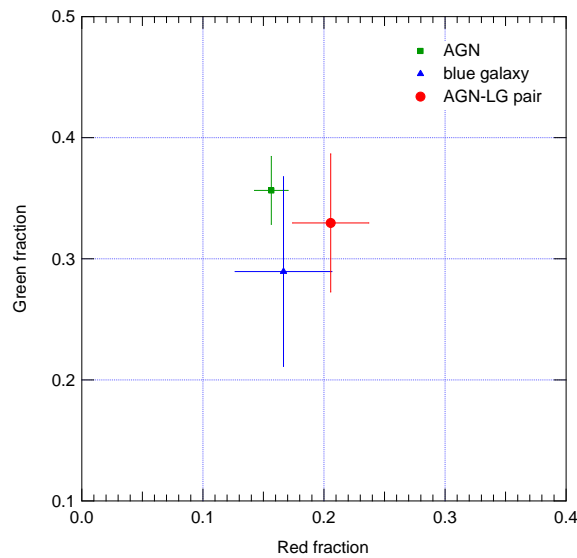


Fig. 11. Fractions of red and green galaxies obtained for the three samples.

4.3 Absolute magnitude distribution

To investigate the difference in the luminosity function of the galaxies clustered around the three target types, we derived the absolute magnitude distributions within the region of 0.2–2.0 Mpc from the targets, as applied for the color in the previous section. They were derived separately for two galaxy types, namely, the blue and red galaxy types. The blue types were selected by their color $D < 1.4$, and the red types were selected using $D \geq 1.4$. Because the color distribution of a green-type galaxy overlaps significantly with those of the red- and blue type-galaxies, we simply divided the data into two galaxy types. The absolute magnitude of each HSC source was calculated according to the method described in section 3.2.

The absolute magnitude distributions derived were corrected for their completeness including the reduction from the photo- z selection. To estimate the reduction rate by the photo- z selection as a function of the absolute magnitude, we compared the magnitude distribution obtained for all galaxies (without photo- z selection) with that for the photo- z selected galaxies of the whole AGN sample. The results are shown in figure 12. The top panel of the figure shows the comparison between the two galaxy samples, and the bottom panel shows the ratio of the photo- z selected galaxies to all galaxies.

We assumed that the reduction rate for the red galaxy type is constant for the entire range of magnitude. The measured ratios are consistent with this assumption and the average ratio obtained was 0.665. In the case of the blue galaxy type, the rate of reduction decreases on the fainter side, as shown in the bottom panel of figure 12, and thus we interpolated the ratios using an analytic function, such that it increase to the average ratio given for the red galaxy type. The interpolation is shown as a solid blue line in the same panel.

Using the reduction rate obtained in this way, we corrected the magnitude of the distributions derived from the photo- z selected galaxies for the three target types. The results are shown in figure 13. The plots are only shown in the magnitude range where the completeness exceeds 50%.

The magnitude distributions are fitted with a single Schechter function (Schechter 1976) for the red galaxy type, whereas those for the blue galaxy type are fitted with a combination of two Schechter functions with different parameters. In fitting to the distributions for the red galaxy, we fixed the α parameter of the Schechter function to $\alpha = 0$, which is the average obtained for the three targets by making the α parameter free. The reason of this is to compare M_* among the three samples by fixing the α parameter to the same value. The fitting parameters are summarized in table 9.

Looking at the plot for the blue galaxy sample (middle panel of figure 13), the magnitude

distribution for the blue galaxy type flattens at approximately $M_{\lambda 310} \sim -20$ and steepens again at approximately $M_{\lambda 310} \sim -21$. To reproduce this feature, we assumed two components, one of which is characterized using the Schechter function with a larger (fainter) characteristic magnitude M_* and slope parameter $\alpha = -1.2$, and the other is characterized with a smaller (brighter) M_* and flat slope parameter $\alpha = 0$, which is the parameter used for the red galaxy type. In the cases of the whole AGN and AGN-LG samples, the secondary component with the brighter M_* parameter dominates over the primary component at magnitudes $M_{\lambda 310} < -19$. Because of that, the parameter M_* for the primary component was not well constrained, and thus the M_* parameter was fixed to the value obtained for the blue galaxy sample.

In order to test the preference for adding the secondary component, we also fit the absolute magnitude distribution with a single component model and calculated Akaike information criterion (AIC) (Akaike 1974) and Bayesian information criterion (BIC) (Schwarz 1978) for both the single and two component models. The AIC and BIC are information criteria to evaluate the goodness of the statistical model from both the goodness of the fit and complexity of the model, and have been widely applied to astrophysics problems (e.g. Takeuchi 2000; Liddle 2007; Shirasaki et al. 2008).

We used the following formula to calculate the AIC and BIC:

$$AIC = n \ln \left(\frac{\chi^2}{n} \right) + 2k, \quad (6)$$

$$BIC = n \ln \left(\frac{\chi^2}{n} \right) + k \ln(n), \quad (7)$$

where χ^2 , n , and k are normalized residual sum of squares, number of data points, and number of free parameters, respectively. The result of the fitting parameters and obtained AIC and BIC values are summarized in table 10. The result for the two component model is shown in the first row of each target type, and that for the single component model is in the second row where the parameters corresponding to the second component are indicated with dashes.

According to the χ^2 values, both models are acceptable in 90% confidence level for all the samples. If we compare the AIC and BIC values between the two models for each sample, two component model is preferable for the samples of blue galaxy and AGN-LG, and one component model is preferable for the whole AGN sample. This result support introducing the second component to the model as a plausible scenario especially for the case of blue galaxy sample. If this is the case, it is natural to expect that two components exist ubiquitously and there is difference in the mixing ratio depending on the environment. The small difference in the AIC and BIC values for the AGN and AGN-LG samples compared to the blue galaxy

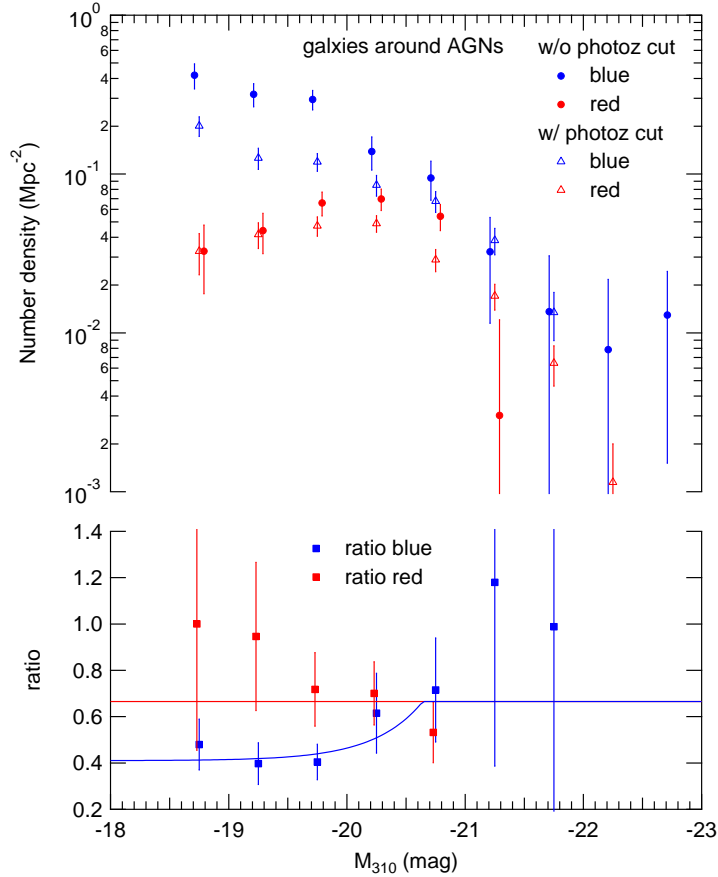


Fig. 12. Top: Absolute magnitude distributions of galaxies around AGNs for the whole AGN sample. The blue and red markers are distributions for the blue and red galaxies, respectively. The distributions shown with solid markers are derived from all galaxies, and those shown with open markers are from the photo- z selected galaxies. Bottom: Ratios for the number of photo- z selected galaxies against all galaxies. A color version is available on-line.

sample can be considered as a result of dominance of secondary component, which is inferred from the two-component fit, in the examined magnitude range. In such a case AIC/BIC will preferentially select the single component model.

The M_* parameters obtained for the red-type galaxy and the secondary component of the blue-type galaxy are shown in figure 14. As indicated in the figure, there are no significant differences in the M_* parameters among the three samples or between the blue and red types. Thus, the difference in the magnitude distribution among the three samples are the fraction of the secondary component in the blue galaxy type and the normalization factor of the luminosity function for each component.

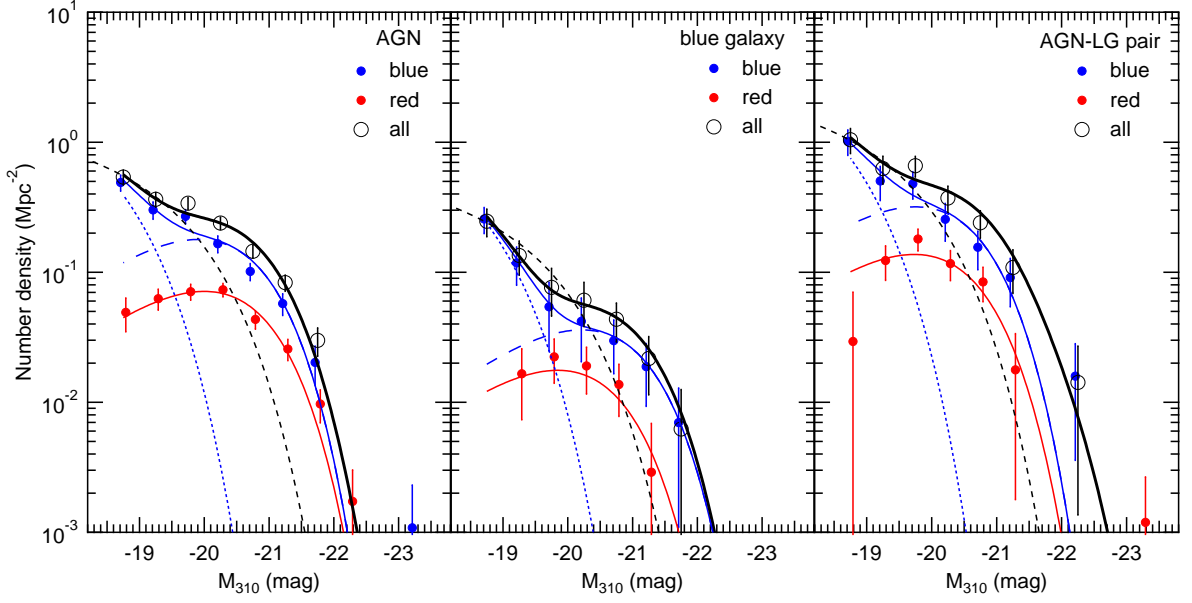


Fig. 13. Absolute magnitude distributions of photo- z selected galaxies around target objects for three samples. The blue (red) closed circles indicate distributions for blue (red) galaxies, and the open circles are for all galaxies. The solid lines represent fitted functions expressed by a Schechter function (for red galaxies) or a combination of two Schechter functions (for blue galaxies). The thick lines represent sum of the functions for blue and red galaxies. The dashed lines represent a model function derived from the luminosity functions described in the literature for $z = 0.95$, which are normalized to the data at $M_{\lambda 310} = -18.75$. The dotted and long dashed lines represent fitted functions corresponding to the primary and secondary components of blue galaxies, respectively. A color version is available on-line.

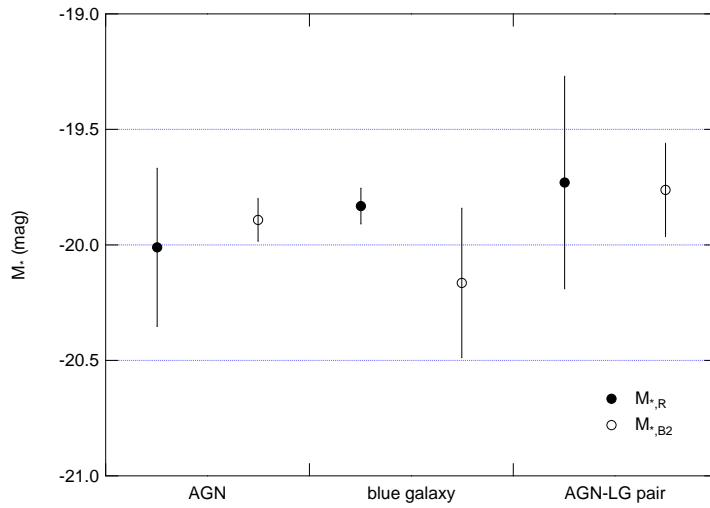


Fig. 14. M_* parameters obtained for secondary component of blue galaxies ($M_{*,B2}$) and for red galaxies ($M_{*,R}$).

Table 9. Fitting result for absolute magnitude distribution of red

galaxies.

target type	ϕ_R^a	α_R^b	$M_{*,R}^c$	χ^{2d}	n^e
AGN	0.026 ± 0.003	0.0	-20.0 ± 0.07	3.59	7
blue galaxy	0.007 ± 0.003	0.0	-19.9 ± 0.27	5.54	7
AGN-LG pair	0.062 ± 0.013	0.0	-19.7 ± 0.15	5.53	7

^a number density at $M_{\lambda 310} = -18$. ^b α parameter of the Schechter function. This was fixed to 0.0. ^c M_* parameter of the Schechter function. ^d normalized residual sum of squares, ^e number of data points.

Table 10. Fitting result for absolute magnitude distribution of blue galaxies.

target type	ϕ_{B1}^a	α_{B1}^b	$M_{*,B1}^c$	ϕ_{B2}^a	α_{B2}^b	$M_{*,B2}^c$	χ^{2d}	n^e	k^f	AIC^g	BIC^h
AGN	0.96 ± 0.17	-1.2	-18.3	0.070 ± 0.012	0.0	-19.90 ± 0.09	6.50	7	3	5.5	5.3
	0.50 ± 0.05	-1.2	-20.6 ± 0.12	-	-	-	3.24	7	2	-1.4	-1.5
blue galaxy	0.56 ± 0.29	-1.2	-18.3 ± 0.56	0.011 ± 0.008	0.0	-20.2 ± 0.35	0.05	7	4	-26.6	-26.8
	0.19 ± 0.05	-1.2	-20.4 ± 0.31	-	-	-	6.23	7	2	3.2	3.1
AGN-LG pair	1.84 ± 0.58	-1.2	-18.3	0.142 ± 0.054	0.0	-19.7 ± 0.20	2.13	7	3	-2.3	-2.5
	1.02 ± 0.18	-1.2	-20.3 ± 0.23	-	-	-	3.28	7	2	-1.3	-1.4

^a number density at $M_{\lambda 310} = -18$ for the primary (B1) and secondary (B2) components. ^b α parameter of the Schechter function for the primary (B1) and secondary (B2) components. they are fixed to -1.2 and 0.0, respectively. ^c M_* parameter of the Schechter function for the primary (B1) and secondary (B2) components. $M_{*,B1}$ of AGN and AGN-LG pair are fixed to -18.3, which is the value obtained for blue galaxy. ^d normalized residual sum of squares. ^e number of data points. ^f number of free parameters. ^g Akaike information criterion. ^h Bayesian information criterion.

4.4 Stellar mass distribution

Stellar mass distributions around the target objects for three samples were derived using the photo- z selected HSC sources with absolute magnitude of $M_{\lambda 310} < -19$. Figure 15 shows a comparison between them. The top panel shows the number densities at distances of 0.2–2.0 Mpc from the target objects, which were obtained by subtracting the density distribution at 7–9.8 Mpc from that at 0.2–2.0 Mpc. The bottom panel shows the ratios to the number densities obtained for the whole AGN sample.

It can clearly be seen that HSC sources around the targets in the whole AGN and AGN-LG samples have a higher relative density than those in the blue galaxy sample at stellar masses of $M_* \geq 10^{10} M_\odot$. The ratios for the blue galaxy sample shows a decreasing trend at above $10^{9.6} M_\odot$. There is no significant difference in the ratios for the AGN-LG sample.

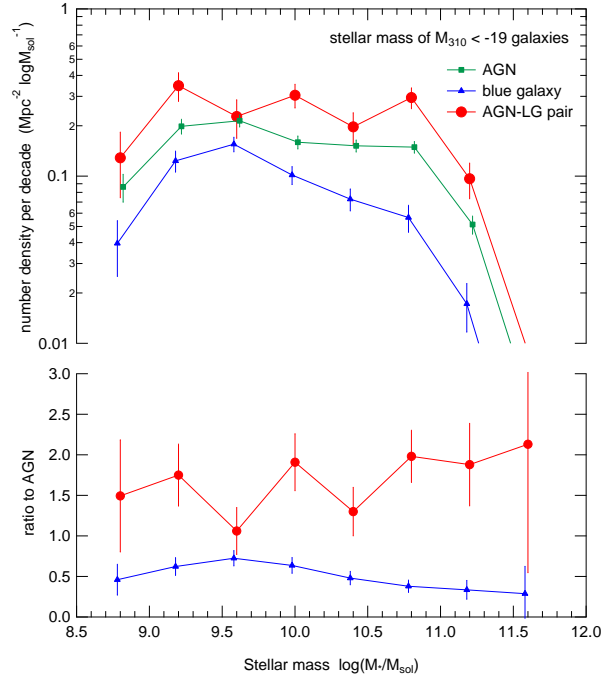


Fig. 15. Top: Stellar mass distribution of galaxies around target objects of three samples. Bottom: Ratios of the densities to those measured for the whole AGN sample.

4.5 positional distribution of clusters

In previous sections, we compared the properties of the environment for three samples based on the properties of individual HSC sources, i.e., galaxies. In this and the following sections, we investigate the properties of their environment focusing on the clusters of the HSC sources.

The method used to find clusters is described in section 3.3. In creating the stellar mass or number density map, we used photo- z selected HSC sources with a magnitude of $M_{\lambda 310} < -19$ mag. We selected clusters based on two density maps: one is a map of the stellar mass density and the other is a map of the source number density.

Figure 16 shows the radial number density distributions of clusters found in the stellar mass density map (mass peak clusters, left-hand panel) and clusters found in the number density map (number peak clusters, right-hand panel). The threshold for the counting cluster was set to peak densities of $10^{10.8} M_{\odot} \text{Mpc}^{-2}$ and $10^{1.6} \text{Mpc}^{-2}$, respectively. These numbers correspond to the detection threshold for clusters by this method as will be shown in figure 18 of the next section. The average cluster density at a projected distance of 4 to 7 Mpc are subtracted from the density distribution. In each panel, the distributions for the three samples are compared. The uncertainties of the number density are derived based on the Poisson statistics and the error bars denote one sigma uncertainty.

The distributions of the mass peak clusters show an excess over the average at < 1.2 Mpc, and the excess density increases toward the target objects for the cases of the whole AGN and AGN-LG samples. The significance of the excess is 7.1 and 2.9 sigma for the whole AGN and AGN-LG samples, respectively. The excess is smaller and less significant (2.8 sigma) for the case of the blue galaxy sample.

The distributions of the number peak clusters show a significant excess at < 1.2 Mpc distances for all three samples. The significance of the excess is 6.8, 2.6, and 7.3 sigma for the whole AGN, AGN-LG, and blue galaxy samples, respectively. The number density distributions are almost identical among the three samples. The average number of clusters that have a peak number density of $> 10^{1.6} \text{Mpc}^{-2}$ and are found at a distance of < 1.2 Mpc from the target objects is 0.15. Thus, for $\sim 85\%$ of the target objects, clusters above the threshold are unassociated with them.

To investigate whether isotropy occurs in the distribution of the clusters in environments of AGN-LG pairs, we derived a density map for the distribution of the clusters in a reference frame defined by the position of the AGN and LG. The origin of the AGN-LG reference frame was set at the location of the AGN, and the direction from the AGN to LG was defined as the x -axis direction. The distance was then scaled such that the distance between the AGN and LG was normalized to five in the reference frame. The y -axis was defined as the projected scaled-distance from the AGN-LG axis.

By transforming the positions of all clusters to the AGN-LG reference frame, they are plotted with solid circles in figure 17. The top panel is for the mass peak clusters and the bottom panel is for the number peak clusters. The contours and color map were calculated by taking a convolution with a 2D Gaussian with $\sigma = 1$, as is applied when finding the cluster peaks.

In both plots, a concentration of clusters around the AGN located at (0,0) and around the LG at (5,0) is clearly seen. Looking at the positional distribution of the mass peak clusters (top panel of the figure), a weak feature elongated toward the vertical direction of the AGN-LG axis is indicated.

For the number peak cluster (bottom panel of the figure), the elongation is not clear at the position of LG ($x = 5$) but is seen at the AGN position ($x = 0$). As a more outstanding feature, the peak of the concentration near the AGN is shifted toward the LG position.

To evaluate the significance of the anisotropy around the AGNs, we carried out a Monte Carlo simulation for the distribution of clusters in the AGN-LG frame. The simulation was conducted for each dataset of AGN-LG pairs by assuming the power law plus constant density

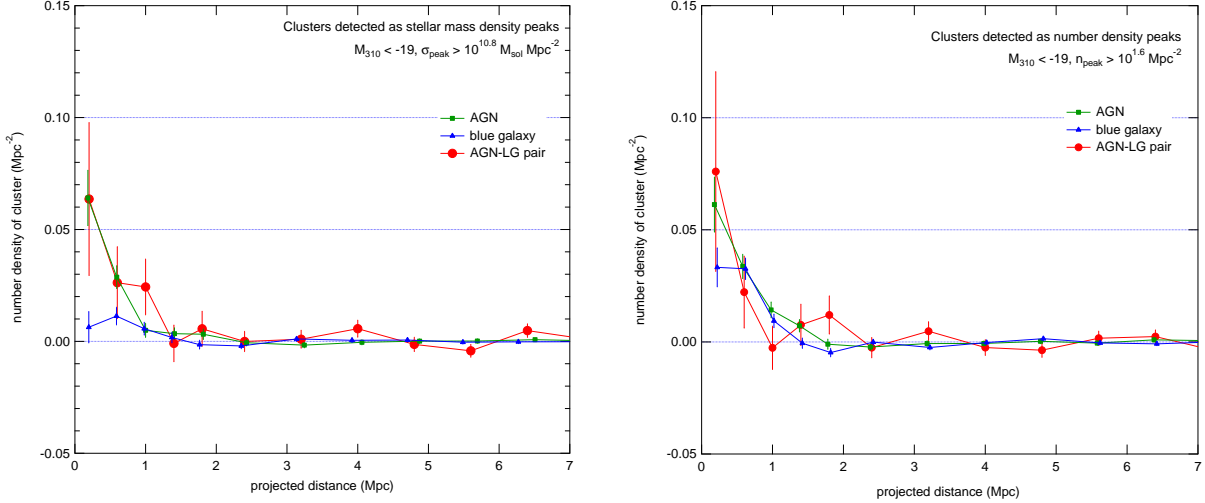


Fig. 16. Left: radial distributions of clusters detected as stellar mass density peaks for three samples. Offset (background) densities measured at 4–7 Mpc were subtracted. Right: Same plot as the left panel for clusters detected as the number density peaks.

distribution for clusters, as measured in the right panel of figure 16. The simulated positions of the clusters were converted into an AGN-LG frame according to the real positions of the AGN and LG. The ratios of the number count at the LG side ($x = 0 - 2, y < 2$) to the count at the anti-LG side ($x = -2 - 0, y < 2$) were then measured. These numbers for the real observation are 26 at the LG side and 11 at the anti-LG side, and thus the ratio is 0.70.

Among the 1000 sets of simulated samples, the maximum ratio was 0.61. Comparing this value with the real observed value of 0.70, the probability of obtaining the observed anisotropy was estimated to be less than 0.1%.

This anisotropy can be attributed to the overlap of clusters associated with the AGN and LG. Such an offset is not significant in the distribution of clusters detected as mass peaks, which may be due to a larger mass density for clusters associated with AGNs than clusters associated with LGs.

4.6 Peak density of clusters

To investigate the properties of the clusters associated with the target objects, we derived the distribution of peak densities for mass peak clusters and number peak clusters, in the same way as conducted for the color, absolute magnitude, and stellar mass described in the previous sections. In deriving the distributions, a high-density region was taken at < 1 Mpc and a low-density region was considered at 2–6 Mpc.

The left panel of figure 18 shows the distribution of peak densities of the mass peak clusters, which demonstrates an excess of approximately $\sigma_{\text{peak}} = 10^{10.8} - 10^{11.6} M_{\odot} \text{Mpc}^{-2}$. The

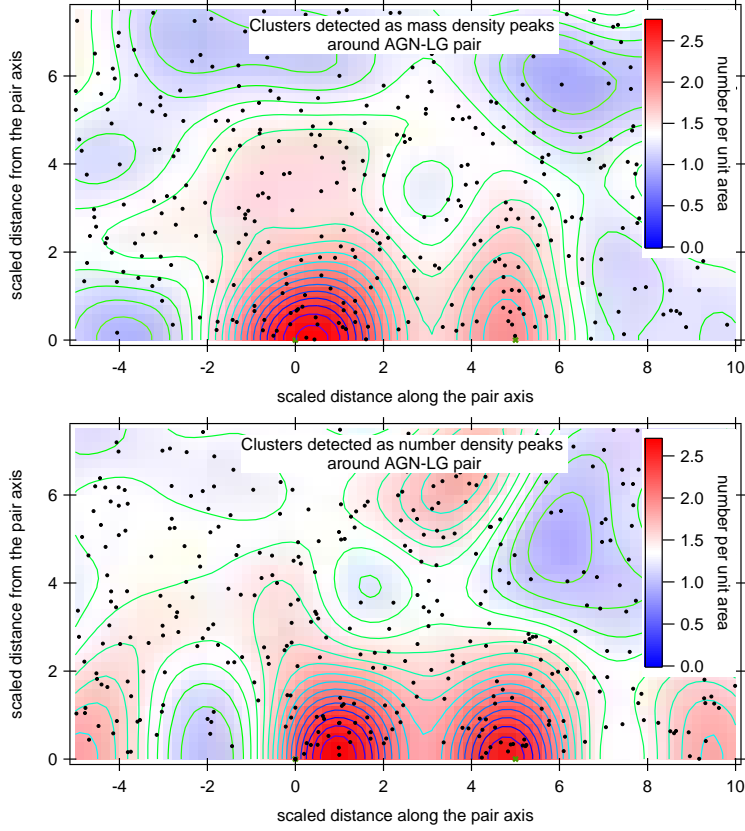


Fig. 17. Distributions of clusters in the AGN-LG frame. The top panel is for clusters found as the stellar mass density peaks, and the bottom panel is for clusters found as the number density peaks. XY axes are scaled so that the the AGN and LG are located at (0,0) and (5,0), respectively. The contours of the number density are drawn at a step of 0.1 per unit area.

excess densities for the whole AGN and AGN-LG samples are larger than those for the blue galaxy sample at all peak densities. No significant difference is seen in the excess densities between the whole AGN and AGN-LG samples.

The right panel of the figure 18 shows the distribution of peak densities of the number peak clusters. The excess densities for the whole AGN and blue galaxy samples are almost identical at below $n_{\text{peak}} < 10^{1.8} \text{Mpc}^{-2}$. At higher peak densities, a decreasing trend is shown in the ratios of density for the blue galaxy to whole AGN. The excess densities for the AGN-LG sample are consistent with those of both the whole AGN and blue galaxy samples within the statistical error at $> 10^{1.7} \text{Mpc}^{-2}$.

A depletion at $10^{1.6} - 10^{1.7} \text{Mpc}^{-2}$ for the AGN-LG sample can be seen, where no cluster was found at $< 1 \text{Mpc}$ whereas ~ 5 clusters were expected. This may be due to the anisotropy of cluster distributions around the AGN of the AGN-LG pairs, as the position of cluster is shifted toward the LG direction.

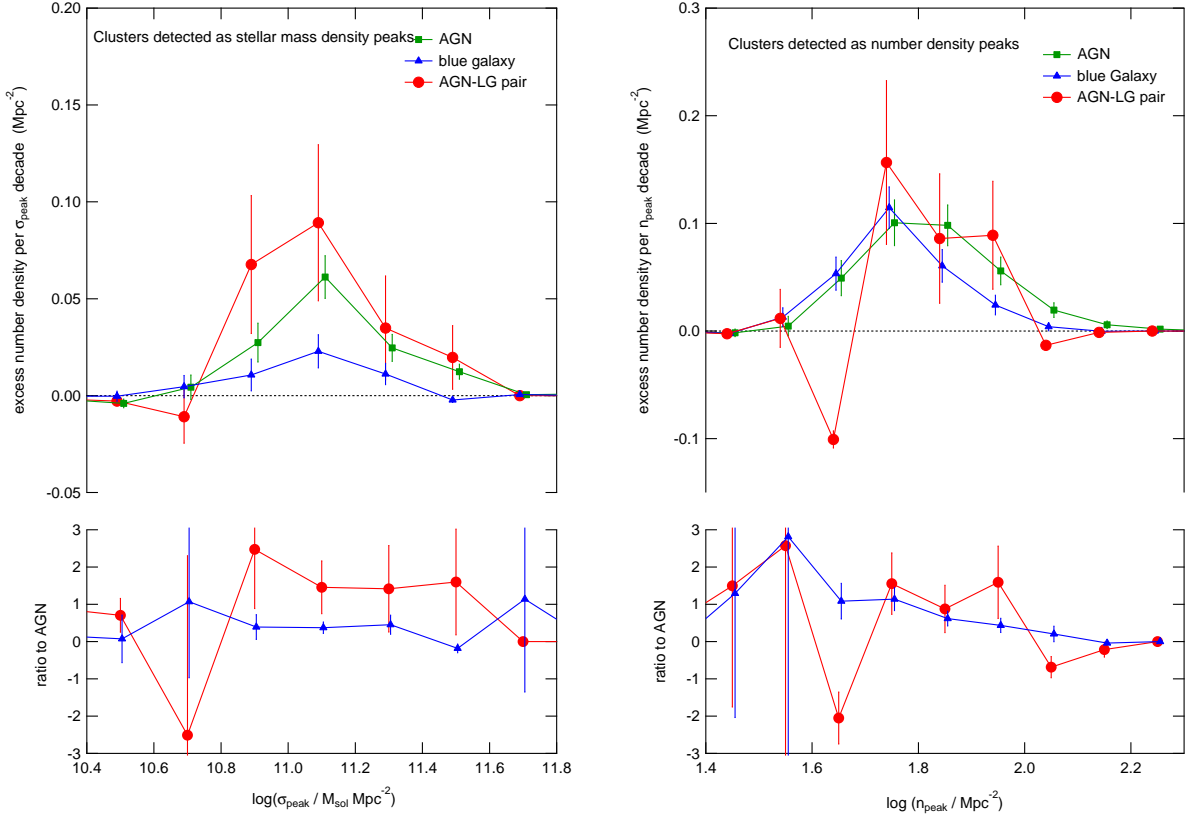


Fig. 18. Left: Distributions of peak stellar mass density for three samples. The ratios to the densities measured for the whole AGN sample are plotted in the bottom panel. Right: Same plot as the left panel for the peak number density.

4.7 Number distribution of cluster

According to the results of the positional distribution of the clusters in the AGN-LG frame, multiple clusters that are associated with the AGN and LG are expected to exist in the environment near the AGN-LG pair. To test this, we compared the number distribution of clusters found within a 5 Mpc distance from the target objects. The distance scale of 5 Mpc was chosen to count clusters located within 1 Mpc from the LG, which is separated by 4 Mpc from the AGN at maximum. The thresholds of the peak density were set to $10^{11} M_{\odot} \text{Mpc}^{-2}$ and $10^{1.8} \text{Mpc}^{-2}$ for the mass peak clusters and number peak clusters, respectively. These thresholds approximately correspond to the peak density of the distribution as is shown in figure 18.

Figure 19 shows the normalized distributions of the number of clusters for the three samples. The left panel is for the mass peak clusters and the right panel is for the number peak clusters. In both cases, there is no significant difference between the distributions for the AGN and blue galaxy samples, whereas the distributions for the AGN-LG sample are slightly shifted to a larger number.

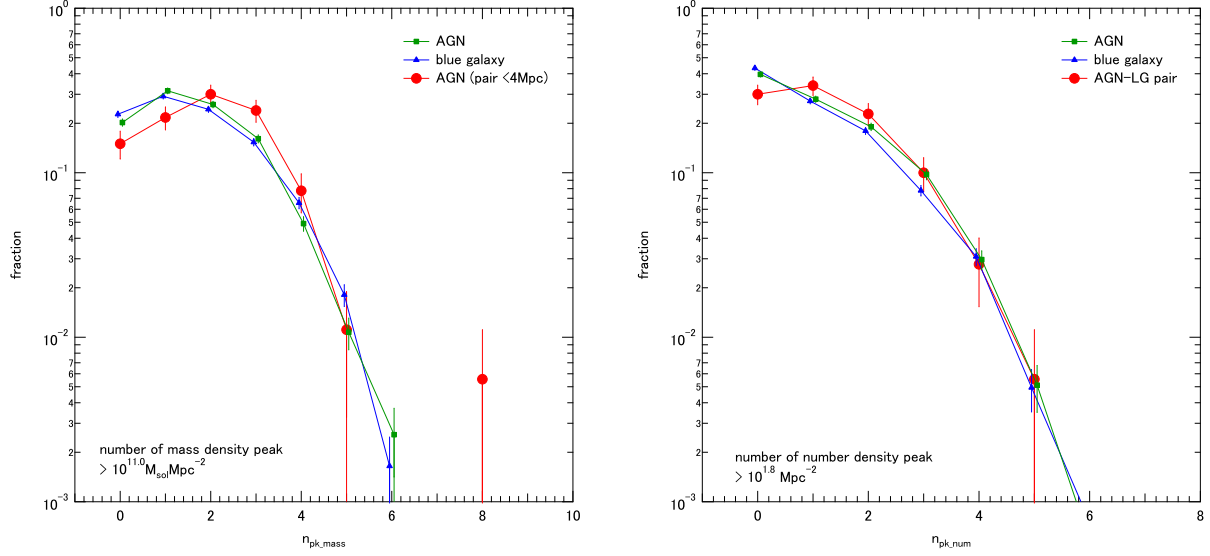


Fig. 19. Left: Normalized distribution of number of clusters detected as stellar mass density peaks and found at <5 Mpc from the target objects. The threshold peak density was set to $10^{11.0} M_{\odot} \text{Mpc}^{-2}$. Right: Same plot for clusters detected as the number density peak. The threshold was set to $10^{1.8} \text{Mpc}^{-2}$.

The average numbers of clusters per field are plotted in figure 20 for the five samples, including AGN type 1 XR and AGN type 2 samples. We obtained $\langle n_{\text{peak,mass}} \rangle$ ($\langle n_{\text{peak,num}} \rangle$) of 1.58 ± 0.03 (1.10 ± 0.03), 1.60 ± 0.03 (1.02 ± 0.03), 1.94 ± 0.12 (1.23 ± 0.09), 1.68 ± 0.06 (1.17 ± 0.05), and 1.55 ± 0.10 (1.13 ± 0.09) for the whole AGN, blue galaxy, AGN-LG pairs, AGN type 1 XR, and AGN type 2, where $\langle n_{\text{peak,mass}} \rangle$ ($\langle n_{\text{peak,num}} \rangle$) represents the average number of mass peak clusters (number peak clusters).

The average number of mass peak clusters for the AGN-LG sample is 0.34 larger in ~ 3 sigma than that of blue galaxy sample, whereas the difference in the average number of number peak clusters is small and less significant. No significant difference can be seen among the other samples, which is due to the dominance of the foreground and/or background clusters unassociated with the targets. These results indicate an environment in which the AGN-LG pairs has multiple clusters with higher probability than the others has.

5 Discussion

5.1 Comparison of galaxy bias with other measurements

We measured the cross-correlation functions with the HSC sources, i.e., galaxies, for four types of AGN samples, i.e., whole AGNs with a mixture of any type, type 1 AGNs detected in the X-ray and/or radio band (AGN type 1 XR), type 2 AGNs, and AGN-LG pairs, as well as for a blue M_* galaxy sample. For comparison with other observations, we derived a linear bias for

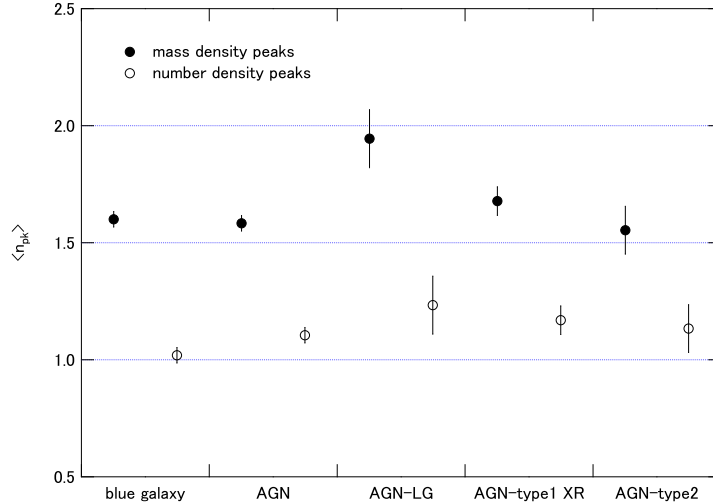


Fig. 20. Average number of clusters found at <5 Mpc from the target objects. Solid circles represent the number for clusters detected as stellar mass density peaks and open circles represent the number for clusters detected as number density peaks.

galaxies clustering around those target objects. We did not attempt to derive the linear bias for AGN itself because of its difficulty arisen from the dominance of the evolved galaxies, which were identified as a flat component in an absolute magnitude distribution, in the AGN fields.

From our previous study (Shirasaki et al. 2018), it is known that there is strong correlation between the AGN and LGs with magnitude brighter than M_* , which is due to the evolution of M_* into the luminous side for galaxies around the AGNs. In this study, we found that this evolution is related to the increase in the fraction of the secondary component in blue and red galaxies (referred to as a flat component collectively), as shown in figure 13. The dominance of the flat component makes it difficult to derive the absolute bias of the AGN from the cross-correlation with galaxies because we need to consider the clustering feature of the flat component. It is also inadequate to assume a simple linear relation between the AGN-galaxy cross-correlation function and auto-correlation functions of the AGN and galaxy, considering that the spatial distribution of the AGNs and the flat component are presumably not independent of each other.

For these reasons, we simply derived the linear bias b_{AG} for the galaxies around AGNs from the cross-correlation length (r_{AG}) and power index (γ) using the following formula (Shirasaki et al. 2018):

$$b_{AG} = \left(\frac{r_{AG}}{8} \right)^{\gamma/2} J_2(\gamma)^{1/2} \left[\sigma_8 \frac{D(z)}{D(0)} \right]^{-1}, \quad (8)$$

where $J_2(\gamma)$ is defined as equation (28) in Shirasaki et al. (2018) and $D(z)$ is the linear growth

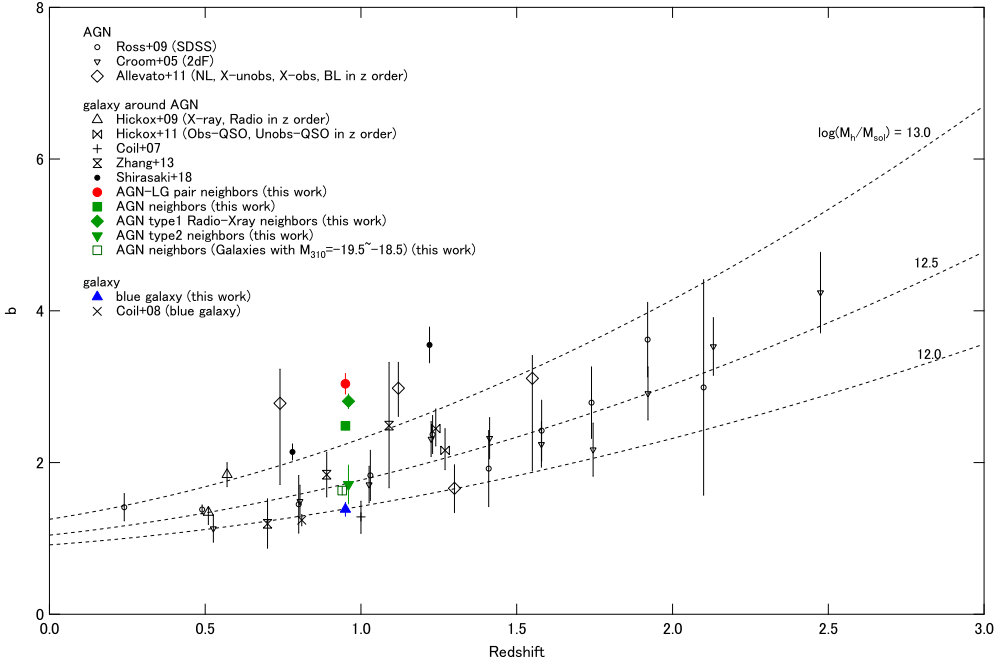


Fig. 21. Conditional absolute biases measured for galaxies ($M_{\lambda 310} < -19$) around five target types: AGN-LG pair, AGN (all types), AGN type 1 XR (X-ray and/or radio detection), AGN type 2 and blue galaxies are plotted as solid markers. A bias calculated for galaxies with $M_{\lambda 310} = -19.5$ — -18.5 around the AGN (all types) is also plotted as an open square. The same bias corresponding to our previous results (Shirasaki et al. 2018) and those obtained from the AGN-galaxy cross-correlation by other authors (Coil et al. 2007; Hickox et al. 2009, 2011; Zhang et al. 2013) are also shown. The absolute biases obtained for the AGN (Croom et al. 2005; Ross et al. 2009; Allevato et al. 2011) and galaxy (Coil et al. 2008) auto-correlation are also plotted. The dashed lines represent a redshift evolution of bias for a DM halo of the given mass, which is calculated in the same way as described in Shirasaki et al. (2018).

factor given as equation (30) in the same literature. The calculated biases for galaxies around the target AGNs and blue galaxies are shown in figure 21 with solid markers, along with those derived from other AGN or galaxy auto-correlation (Croom et al. 2005; Ross et al. 2009; Allevato et al. 2011; Coil et al. 2008) and AGN-galaxy cross-correlation studies (Coil et al. 2007; Hickox et al. 2009, 2011; Zhang et al. 2013; Shirasaki et al. 2018). The biases found in the literature were calculated from the cross-correlation lengths and power index by using equation (8) when they were derived from AGN-galaxy cross-correlation. Because they were derived for galaxies around AGNs, we refer to the bias as a conditional bias of galaxies. The values derived from the AGN/galaxy auto-correlation were drawn from the literature as described.

In the same figure, the expected evolution in bias for DM haloes of different masses are also shown as a reference. We used the relation between dark matter halo mass and bias of the dark matter halo derived by Sheth, Mo, and Tormen (2001). As argued above, the conditional bias is affected by the evolution of galaxies around the AGNs, and should not be used as an estimator for the host DM halo mass. Thus, the large biases obtained for our three AGN samples (whole AGN, AGN type 1 XR, and AGN-LG pair) do not necessarily mean that

they are hosted by DM haloes with $>10^{13}M_{\odot}$.

As a reference, we also calculated the conditional bias for galaxies with absolute magnitudes of $M_{\lambda 310} = -19.5 - -18.5$, where the contribution from the flat component becomes smaller (but not negligible), for the whole AGN sample. The corresponding cross-correlation length is $\sim 4.5 h^{-1}$ Mpc. This is shown in the same figure with an open square, and the bias comes close to that obtained from the AGN auto-correlation (Croom et al. 2005; Ross et al. 2009). If we assume the auto-correlation length of galaxies with those magnitudes to be $\sim 3.8 h^{-1}$ Mpc, which is the value obtained for galaxies around the blue galaxy sample, the auto-correlation length of the AGNs can be calculated as $r_{AA} = r_{AG}^2 / r_{GG} \sim 5.4 h^{-1}$ Mpc assuming the same power index of -1.8 of correlation function. Then the bias is calculated as ~ 1.9 , which is consistent with those obtained by Croom et al. (2005); Ross et al. (2009).

The conditional biases calculated from our previous results (Shirasaki et al. 2018) are also plotted in the same figure (solid black circles) for the $z0$ and $z1$ redshift groups. The bias obtained for the whole AGN sample in this work is consistent with the increasing trend at higher redshifts. The results obtained by Zhang et al. (2013), who adapted an analysis method similar to ours to the SDSS dataset, also show an increasing trend of the conditional biases.

The conditional bias measured for the AGN-LG sample is the largest of our samples, and is nearly the same as the one obtained for the AGN type 1 XR sample within the margin of error. The biases obtained for these two sub-types of AGNs are larger than that obtained for the whole AGN sample, which mostly consists of luminous type 1 AGN/QSO, by more than three sigma.

The over density around AGNs with a radio emission has been reported by numerous authors (e.g. Best et al. 2007; Hickox et al. 2009; Bradshaw et al. 2011). The clustering of X-ray selected AGNs is controversial. Coil et al. (2009) found that X-ray AGNs are more clustered than optically selected QSOs based on the cross-correlation with the same galaxy sample. In contrast, Krumpe et al. (2012) reported that there is no significant difference in the clustering of X-ray selected and optically selected broad-line AGNs. Thus, there seems to be a variety in the clustering of the X-ray selected AGNs, which is probably caused from the sample selection. The X-ray selected AGNs in our AGN type 1 XR sample are likely to reside in high density environment, as the sample is dominated by X-ray selected AGNs as shown in table 3.

Our conditional bias for the blue galaxy sample is consistent with the bias obtained by Coil et al. (2008). In the case of this sample, the contribution from the flat component is almost negligible, and thus the bias obtained is expected to be close to the halo bias. The DM halo mass corresponding to the bias is $M_h \sim 10^{12}M_{\odot}$.

We found a smaller cross-correlation length for the type 2 AGN sample than those for the other AGN samples, which is almost the same as that obtained for the blue galaxy sample. The clustering of type 2 AGNs drawn from the SDSS DR4 was examined by Li et al. (2006), who reported that no significant difference is shown between the type 2 AGNs and a reference sample of galaxies on scales of larger than a few Mpc. Allevato et al. (2011), by contrast, reported a similar bias parameter for both broad-line and narrow-line AGNs selected in the X-ray band. Their measurements of bias are plotted in figure 21, which shows a large bias for the narrow-line AGNs and a relatively smaller bias for X-ray obscured AGNs. Considering the large error bar, it is difficult to draw a conclusive answer to the difference in biases between the AGN types from their measurements.

Hickox et al. (2011) measured the cross-correlation with galaxies for obscured and unobscured QSOs. They argue that the obscured QSOs reside in denser environment than the unobscured QSOs in 1 sigma level. More significant evidence have been obtained by recent works (e.g. DiPompeo et al. 2014, 2017), whereas other authors argue that there is no significant difference between the environments of obscured and unobscured (or type 1 and type 2) QSOs (e.g. Mendez et al. 2016). Based on the clustering analysis for AGNs at the local Universe, several authors have reported that obscured AGNs (or type 2 AGNs) reside in denser environment than unobscured (or type 1 AGNs) (e.g. Powell et al. 2018; Krumpke et al. 2018; Jiang et al. 2016) if it is measured at small scales (< 1 Mpc). Based on the HSC-SSP dataset, Toba et al. (2017) measured the clustering properties of infrared bright dust-obscured galaxies (DOGs), which is thought to be powered by active star formation and/or AGN hidden by surrounding dust, and they report large bias for those populations.

For comparison with our results, conditional biases calculated from the cross-correlation lengths obtained by Hickox et al. (2011) for obscured and unobscured QSOs are plotted in the figure 21. Their biases are significantly smaller than our previous result obtained for whole AGNs at $z = 1.2$ and the extrapolation of this work for whole AGNs along the bias evolution for the same halo mass, whereas the extrapolation of this work for type 2 AGNs is almost consistent with their results. Coil et al. (2009) also reported a smaller bias for the AGN sample as compared to our result for the whole AGN sample at a redshift of ~ 1 . The calculated conditional bias for the AGN sample of Coil et al. (2009) is almost the same as the bias obtained for a blue galaxy in Coil et al. (2008).

It is possible that the inconsistency between their results and ours comes from the difference in the estimation of the average number density of the correlated galaxies. In our analysis the galaxy density is estimated from the model of the luminosity function, which was

derived from the luminosity functions obtained by several deep surveys. Because the statistics are usually low for galaxies at the luminous end of the luminosity function derived from deep surveys, the flattening of the luminosity function at $< M_*$ owing to the emergence of the flat component, as observed in this study, could be completely missed.

This leads our analysis to an underestimation of the average number density of galaxies, which results in a higher cross-correlation with bright galaxies. In studies by Hickox et al. (2011) and Coil et al. (2007), the average number density is estimated from the galaxy sample itself, and the sample usually has sufficient statistics for detecting a flat component. Despite the possible uncertainty in the estimation of the average number density in our analysis, it is expected to be small considering the consistency found for a blue galaxy sample between ours and Coil et al. (2008). Thus, the inconsistency could be due to the difference in the sample selection for the AGNs and/or galaxies.

Although there is a difficulty in comparing with other works carried out using different methods and samples, a reliable comparison is possible if it is made under the same method and same galaxy sample. The differences found between our different target samples are more reliable, because they were compared under the same conditions to the greatest extent possible. In the next section we discuss the properties of the environment around AGN-LG pairs based on the results derived from fair comparisons.

5.2 Properties of the environment around AGN-LG pairs

As already discussed in the previous section, the environment around AGN-LG pairs is characterized as a high-density region if compared in a high luminosity range ($M < M_*$). The projected cross-correlation function is as large as that of AGNs with a radio and/or X-ray emission, which have been known to be located in a higher density region compared to the other type of AGNs. As shown in figure 4, the luminosity of the AGNs in the AGN-LG pair sample is relatively lower than those in the whole AGN sample. One possible reason for this is that the AGNs in the AGN-LG pair sample are dominated by AGNs obscured by their surrounding dust to a certain degree. There have been several studies suggesting that obscured AGNs tend to reside in denser regions than unobscured AGNs (e.g. Hickox et al. 2011; DiPompeo et al. 2014, 2017; Powell et al. 2018). Another possibility is the contribution of intrinsically less luminous AGNs, which are driven by, e.g., a quiescent accretion of hot halo gas (Kereš et al. 2009; Fanidakis et al. 2013).

We also found the excess in the average number of mass peak clusters for the AGN-LG

sample (figure 20) against those measured for the other samples. In addition to this, we also found that the positional distribution of the number peak clusters departs from an isotropic distribution around each AGN and LG when they are measured in the AGN-LG pair frame (bottom panel of figure 17). These results indicate that, for a portion of the AGN-LG pairs, at least two clusters are located around them.

The luminosity function of blue galaxies at distances of less than 2 Mpc from the AGNs of the AGN-LG pairs was measured, and it can be better expressed with a linear combination of two Schechter functions with different M_* and α values, as shown in figure 13. The component characterized with a larger (fainter) M_* (primary component) is a main component at magnitudes fainter than $M_{\lambda 310} = -19$ mag. The other component (secondary component), which dominates at magnitudes brighter than $M_{\lambda 310} = -20$ mag, is characterized with a smaller (brighter) M_* and a flat slope parameter of $\alpha \sim 0$.

The luminosity function of red galaxies was also measured, and it is likely to have similar characteristics with the secondary component found in the luminosity function of the blue galaxies. Thus, both components are presumably produced by a common mechanism, and we refer to them as a flat component hereafter. The same features are also found for galaxies in the other two samples, i.e., whole AGN and blue galaxy samples.

Comparing the ratios of the number density of the secondary component of blue galaxies ϕ_{B2} to that of the primary component ϕ_{B1} (table 10), they are almost the same (0.078 ± 0.014 for whole AGN and 0.075 ± 0.023 for AGN-LG pair), whereas the fraction for the blue galaxy (0.021 ± 0.018) is significantly smaller than that of the other two samples.

The comparison of the stellar mass distributions around the targets among the three samples shows flatter distributions at larger stellar masses for the AGN and AGN-LG than that for the blue galaxy (figure 15). This can be explained by the higher fraction of the flat component, which are typically luminous and thus have a larger stellar mass, for the AGN and AGN-LG samples.

These results indicate that some type of AGN preferentially occurs in an environment in which galaxies are rapidly evolving toward a red sequence. The flat component of blue galaxies could be the intermediate state of a galaxy evolving toward a red sequence galaxy considering the similarity between the luminosity functions.

We were unable to find any significant difference in the properties of clusters for the AGN and AGN-LG pair samples within the immediate environment of <1 Mpc from the AGNs. The clustering of clusters around the AGN are nearly the same for both samples (figure 16), and the distributions of peak density of the mass peak clusters and number peak clusters are also

identical within the statistical error (figure 18). A difference is seen if they are compared at a larger scale.

For the AGN-LG sample, we found that the average number of mass peak clusters at < 5 Mpc from the AGNs is larger than those for the other samples (figure 20), which indicates that the large clustering of LGs, i.e., the emergence of a flat component for the AGN-LG pairs, is related with the larger clustering of DM haloes at a scale of several Mpc. For the AGN type 1 XR sample, by contrast, we were unable to find a significant difference in the number of mass peak clusters from the other samples, i.e., whole AGN, blue galaxy, and AGN type 2 samples. This might be explained as two clusters being located too close to be identified as separate mass peak clusters or already merged into a single large cluster in the environment of AGN type 1 XR. At any rate, the existence of multiple clusters around AGN-LG pairs indicates that there is some cluster-scale mechanism invoking AGN activity and evolution of surrounding galaxies simultaneously.

There is an argument that LGs are known to be highly clustered thus the environment of the AGN-LG pairs consequently should be a high density region and have higher probability of association of nearby clusters. This argument, however, is not adequate in explaining why there is a large cross-correlation between AGN and LG separated by several Mpc, which is an original question raised at the start of this work. We argue, instead, that the large-scale interaction of clusters could be a primary driver for producing AGNs and luminous galaxies in the restricted regions, which leads to the strong cross-correlation between them. Our observational results support this argument.

6 Summary and conclusion

We investigated the properties of the environment around pairs of AGN and luminous galaxies (AGN-LG pairs) to understand what causes the strong correlation between AGNs and LGs found in Shirasaki et al. (2018). From a comparison of the environmental properties measured for four AGN samples, (whole AGN, AGN-LG, AGN type 1 XR, and AGN type 2 samples) and one blue galaxy sample, the following information was obtained:

1. AGNs are preferentially located at the environment where luminous galaxies ($M < M_*$) are enriched compared to the environment of blue M_* galaxies. The measured cross-correlation lengths with galaxies ($M_{\lambda 310} < -19$) are $7.22 \pm 0.16 h^{-1} \text{Mpc}$ and $3.77 \pm 0.27 h^{-1} \text{Mpc}$ for the whole AGN and blue galaxy samples, respectively. All cross-correlation lengths are calculated for $\gamma = 1.8$.

2. The environment of type 2 AGNs is similar to that of blue M_* galaxies. The measured cross-correlation length is $4.77 \pm 0.78 h^{-1} \text{Mpc}$ for the AGN type 2 sample.
3. The luminosity of the AGNs in the AGN-LG sample is typically lower than that of the whole AGN sample, which may indicate that they are dominated by obscured and/or intrinsically less luminous AGNs.
4. AGNs in the AGN-LG sample are located in an environment of slightly higher density than those in the whole AGN sample. The measured cross-correlation length is $9.03 \pm 0.44 h^{-1} \text{Mpc}$ for the AGN-LG sample. The cross-correlation is almost equivalent to that obtained for AGN type 1 (RX) sample, which is $8.27 \pm 0.31 h^{-1} \text{Mpc}$.
5. The cross-correlation length of AGNs with fainter galaxies comes close to that measured for blue galaxies. This indicates that the mass of the dark matter halo hosting AGNs is not particularly high but is at most a few times as large as that of the hosting blue galaxies.
6. The luminosity functions around the AGNs and blue galaxies are expressed by a linear combination of two Schechter functions: one represents the primary component at a faint end $M > M_*$, and the other one represents a flat component characterized by a flat slope parameter ($\alpha \sim 0$) and brighter M_* than that of the primary component.
7. The ratio of the flat component to the primary component measured at $M_{\lambda 310} = -18$ is three-times higher in an AGN environment than in a blue galaxy environment. The larger cross-correlation lengths obtained for the AGN samples are mostly due to an enhancement of the flat component.
8. As expected from the enhancement of the flat component, which is characterized by bright, and hence a large stellar mass, an enrichment of large stellar mass galaxies was measured around the AGNs as compared to around the blue galaxies.
9. The clustering of clusters detected as stellar mass density peaks (mass peak clusters) is larger around the AGNs than that around the blue galaxies, whereas the clustering of clusters detected as the number density peaks (number peak clusters) are almost the same between them. No statistically significant difference is shown between the whole AGN and AGN-LG samples.
10. The clustering of the mass peak cluster around the AGNs is almost equally larger at any peak density of clusters than that around the blue galaxies. A clustering of number peak clusters around the AGNs is similar for a smaller peak density ($< 10^{1.8} \text{Mpc}^{-2}$), and becomes larger at a larger peak density ($\geq 10^{1.8} \text{Mpc}^{-2}$). No statistically significant difference is shown between the whole AGN and AGN-LG samples.
11. The anisotropic distribution of clusters was found in an environment of AGN-LG pairs if

measured in the AGN-LG frame. We found that the peak position of the number peak clusters near the AGNs is shifted toward the LG direction, which indicates the coexistence of two clusters around the AGN-LG pairs.

12. An excess average number of mass peak clusters was found for the AGN-LG sample against the other samples, which again indicates the enhancement of the number of clusters in the AGN-LG pair environments.

Based on these findings, the following scenario regarding to the evolution of an AGN and a galaxy can be drawn: AGNs, at least some classes of AGNs, are preferentially produced in an environment in which the number density of dark matter haloes is relatively high. In such an environment, a star formation is ignited in multiple galaxies by a large-scale mechanism related with the multiple dark matter haloes, and then evolves through green valley galaxies with a quenched star formation, finally becoming red sequence galaxies. An AGN is an episodic event produced along with a galaxy evolution, and thus the strong correlation of an AGN and luminous galaxies is a natural consequence in such an environment. Collisions and/or interaction of dark matter haloes is a possible mechanism facilitating such a galaxy evolution at a large scale.

Acknowledgments

We would like to thank the anonymous referee for the constructive feedback, which helped us in improving the paper. This work is based on data collected at the Subaru Telescope and retrieved from the HSC data archive system, which is operated by Subaru Telescope and Astronomy Data Center, National Astronomical Observatory of Japan. The Hyper Suprime-Cam (HSC) collaboration includes the astronomical communities of Japan and Taiwan, and Princeton University. The HSC instrumentation and software were developed by the National Astronomical Observatory of Japan (NAOJ), the Kavli Institute for the Physics and Mathematics of the Universe (Kavli IPMU), the University of Tokyo, the High Energy Accelerator Research Organization (KEK), the Academia Sinica Institute for Astronomy and Astrophysics in Taiwan (ASIAA), and Princeton University. Funding was contributed by the FIRST program from Japanese Cabinet Office, the Ministry of Education, Culture, Sports, Science and Technology (MEXT), the Japan Society for the Promotion of Science (JSPS), Japan Science and Technology Agency (JST), the Toray Science Foundation, NAOJ, Kavli IPMU, KEK, ASIAA, and Princeton University. This paper makes use of software developed for the Large Synoptic Survey Telescope. We thank the LSST Project for making their code available as free software at <http://dm.lsst.org>. The Pan-STARRS1 Surveys (PS1) have been made possible through contributions of the Institute for Astronomy, the University of Hawaii, the Pan-STARRS Project Office, the Max-Planck Society and its participating institutes, the Max Planck Institute for Astronomy, Heidelberg and the Max Planck Institute for Extraterrestrial Physics, Garching, The Johns Hopkins University, Durham University, the University of Edinburgh, Queen's University Belfast, the Harvard-Smithsonian Center for Astrophysics, the Las Cumbres Observatory Global Telescope Network Incorporated, the National Central University of Taiwan, the Space Telescope Science Institute, the National Aeronautics and Space Administration under Grant No. NNX08AR22G issued through the Planetary Science Division of the NASA Science Mission Directorate, the National Science Foundation under Grant No. AST-1238877, the

University of Maryland, and Eotvos Lorand University (ELTE) and the Los Alamos National Laboratory. Funding for the Sloan Digital Sky Survey IV has been provided by the Alfred P. Sloan Foundation, the U.S. Department of Energy Office of Science, and the Participating Institutions. SDSS-IV acknowledges support and resources from the Center for High-Performance Computing at the University of Utah. The SDSS web site is www.sdss.org. SDSS-IV is managed by the Astrophysical Research Consortium for the Participating Institutions of the SDSS Collaboration including the Brazilian Participation Group, the Carnegie Institution for Science, Carnegie Mellon University, the Chilean Participation Group, the French Participation Group, Harvard-Smithsonian Center for Astrophysics, Instituto de Astrofísica de Canarias, The Johns Hopkins University, Kavli Institute for the Physics and Mathematics of the Universe (IPMU) / University of Tokyo, Lawrence Berkeley National Laboratory, Leibniz Institut für Astrophysik Potsdam (AIP), Max-Planck-Institut für Astronomie (MPIA Heidelberg), Max-Planck-Institut für Astrophysik (MPA Garching), Max-Planck-Institut für Extraterrestrische Physik (MPE), National Astronomical Observatories of China, New Mexico State University, New York University, University of Notre Dame, Observatório Nacional / MCTI, The Ohio State University, Pennsylvania State University, Shanghai Astronomical Observatory, United Kingdom Participation Group, Universidad Nacional Autónoma de México, University of Arizona, University of Colorado Boulder, University of Oxford, University of Portsmouth, University of Utah, University of Virginia, University of Washington, University of Wisconsin, Vanderbilt University, and Yale University. Funding for the DEEP2 Galaxy Redshift Survey has been provided by NSF grants AST-95-09298, AST-0071048, AST-0507428, and AST-0507483 as well as NASA LTSA grant NNG04GC89G. This research uses data from the VIMOS VLT Deep Survey, obtained from the VVDS database operated by Cesam, Laboratoire d'Astrophysique de Marseille, France. This paper uses data from the VIMOS Public Extragalactic Redshift Survey (VIPERS). VIPERS has been performed using the ESO Very Large Telescope, under the "Large Programme" 182.A-0886. The participating institutions and funding agencies are listed at <http://vipers.inaf.it> Funding for PRIMUS is provided by NSF (AST-0607701, AST-0908246, AST-0908442, AST-0908354) and NASA (Spitzer-1356708, 08-ADP08-0019, NNX09AC95G). This research has made use of NASA's Astrophysics Data System. This research has made use of the VO service toolkit developed by the Japanese Virtual Observatory group at ADC, NAOJ. We would like to thank to the members of HSC AGN WG for a fruitful discussion. We would like to thank Editage (<http://www.editage.com>) for editing the first version of a manuscript for English language.

References

- Abolfathi, B. et al. 2018, *ApJS*, 235, 42
- Aihara, H., et al. 2017, *PASJ*, 70, S4,
- Aihara, H., et al. 2019, *PASJ*, in press, arXiv:1905.12221 [astro-ph.IM]
- Akaike, H. 1974, *IEEE Transaction on Automatic Control*, 19, 716
- Allevato, V., et al. 2011, *ApJ*, 736, 99
- Allevato, V., et al. 2014, *ApJ*, 796, 4
- Axelrod, T., Kantor, J., Lupton, R. H., & Pierfederici, F. 2010, *Proceedings of the SPIE*, 7740, 774015.
- Best, P. N., von der Linden, A., Kauffmann, G., Heckman, T. M., & Kaiser, C. R., 2007, *MNRAS*, 379, 894
- Bosch, J., et al., 2018, *PASJ*, 70S, 5
- Bradshaw, E. J., et al. 2011, *MNRAS*, 415, 2626
- Brammer, G. B., van Dokkum, P. G., & Coppi, P. 2008, *ApJ*, 686, 1503
- Coil, A. L., Hennawi, J. F., Newman, J. A., Cooper, M. C., & Davis, M. 2007, *ApJ*, 654 115
- Coil, A. L., et al. 2008, *ApJ*, 672, 153
- Coil, A. L., et al. 2009, *ApJ*, 701, 1484
- Coil, A. L., et al. 2011, *ApJ*, 741, 8
- Coil, A. L., et al. 2017, *ApJ*, 838, 87
- Cool, R. J., et al. 2013, *ApJ*, 767, 118
- Coupon, J., Czakon, N., Bosch, J., Komiyama, Y., Medezinski, E., Miyazaki, S., & Oguri, M. 2018, *PASJ*, 70, S7
- Croom, S. M., et al. 2005, *MNRAS*, 356, 415
- Di Matteo T., Springel, V., & Hernquist, L. 2005, *Nature*, 433, 604
- DiPompeo, M. A., Myers, A. D., Hickox, R. C., Geach, J. E., & Hainline, K. N. 2014, *MNRAS*, 442, 3443
- DiPompeo, M. A., Hickox, R. C., Eftekharzadeh, S. & Myers, A. D. 2017, *MNRAS*, 469, 4630
- Drinkwater, M. J. et al. 2018, *MNRAS*, 474, 4151
- Fanidakis, N., Macció, A. V., Baugh, C. M., Lacey, C. G., Frenk, C. S. 2013, *MNRAS*, 436, 315
- Fèvre, O. L., et al., 2013, *A&A*, 559, A14
- Flesch, E. W., 2015, *PASA*, 32, 10
- Furusawa, H. et al., 2018, *PASJ*, 70, S3
- He, W., et al. 2018, *PASJ*, 70, S33
- Hsieh, B. C., & Yee, H. K. C. 2014, *ApJ*, 792, 102
- Hickox, R. C., et al., 2009, *ApJ*, 696, 891

Hickox, R. C., et al., 2011, *ApJ*, 731, 117

Hopkins, P. F., Hernquist, L., Cox, T. J., & Kerēs, D. 2008, *ApJS*, 175, 356

Ikedo, H., et al. 2015, *ApJ*, 809, 138

Ivezić, Z., et al. 2008, arXiv:0805.2366 [astro-ph]

Jiang, N., Wang, H., Mo, H., Dong, X, Wang, T. , & Zhou, H. 2016, *ApJ*, 832, 111

Jurić, M., et al. 2015, arXiv:1512.07914 [astro-ph.IM]

Kawanomoto, S., et al., 2018, *PASJ*, 70, 66

Kereš, D., Katz, N., Fardal, M., Davé, R., & Weinberg, D. H. 2009, *MNRAS*, 395, 160

Komiya, Y., Shirasaki, Y., Ohishi, M., & Mizumoto, Y., 2013, *ApJ*, 775, 43

Komiyama, Y. et al., 2018, *PASJ*, 70, S2

Kormendy, J. & Kennicutt, R. C., Jr. 2004, *ARA&A*, 42, 603

Kormendy, J. & Ho, L. C. 2013, *ARA&A*, 51, 511

Krumpe, M., Miyaji, T., Coil, A. L., & Aceves, H. 2012, *ApJ*, 746, 1

Krumpe, M., Miyaji, T., Coil, A. L., & Aceves, H. 2018, *MNRAS*, 474, 1773

Li, C., Kauffmann, G., Wang, L., White, S. D. M., Heckman, T. M., & Jing, Y. P. 2006, *MNRAS*, 373, 457

Liddle, A. R. 2007, *MNRAS*, 377, L74

Magnier, E. A., et al. 2013, *ApJS*, 205, 20

Menci, M., Gatti, M., Fiore, F., & Lamastra, A. 2014, *A&A*, 569, A37

Mendez, A. J., et al. 2016, *ApJ*, 821, 55

Miyazaki, S. et al., 2012, *Proc. SPIE* 8446, 0Z

Miyazaki, S. et al., 2018, *PASJ*, 70S, 1

Newman, J. A., et al. 2013, *ApJS*, 208, 5

Powell, M. C., et al. 2018, *ApJ*, 858, 110

Richstone, D., et al. 1998, *Nature*, 395, A14

Ross, N. P., et al. 2009, *ApJ*, 697, 1634

Sanders, D. B., Soifer, B. T., Elias, J. H., Madore, B. F., Matthews, K., Neugebauer, G. & Scoville, N. Z. 1988, *ApJ*, 325, 74

Schechter, P. 1976, *ApJ*, 203, 297

Schlafly, E. F., et al. 2012, *ApJ*, 756, 158

Schlegel, D. J., Finkbeiner, D. P., & Davis M. 1998, *ApJ*, 500, 525

Schwarz, G. 1978, *Ann. Statist.*, 6, 461

Scodreggio, M., et al., 2018, *A&A*, 609, A84

Sheth, R. K., Mo, H. J., & Tormen, G. 2001, *MNRAS*, 323, 1

Shirasaki, Y., et al. 2008, PASJ, 60, 919
Shirasaki, Y., Tanaka, M., Ohishi, M., Mizumoto, Y., Yasuda, N., & Takata, T. 2011, PASJ, 63, 469
Shirasaki, Y., Komiya, Y., Ohishi, M., & Mizumoto, Y. 2016, PASJ, 68, 23
Shirasaki, Y., et al. 2018, PASJ, 70, S30
Takeuchi, T. T. 2000, *Astrophysics and Space Science*, 271, 213
Tanaka, M., et al. 2018, PASJ, 70, S9
Toba, Y., et al. 2017, *ApJ*, 835, 36
Tonry, J. L., et al. 2012, *ApJ*, 750, 99
Treister, E., Schawinski, K., Urry, C. M., & Simmons, B. D. 2012, *ApJ*, 758, L39
van den Bosch, F. C., Aquino, D., Yang, X., Mo, H. J., Pasquali, A., McIntosh, D. H., Weinmann, S. M., Kang, X. 2008, *MNRAS*, 387, 79
Villforth, C., et al. 2017, *MNRAS*, 466, 812
Zehavi, I., et al. 2011, *ApJ*, 736, 59
Zhang, S., Wang, T., Wang, H., & Hongyan, Z. 2013, *ApJ*, 773, 175